Accelerating the photocatalytic water splitting in catalyst-dye complexes

Shao, Y.

CHAPTER 2

Photocatalytic Water Splitting Cycle in a Catalyst–dye Supramolecular Complex

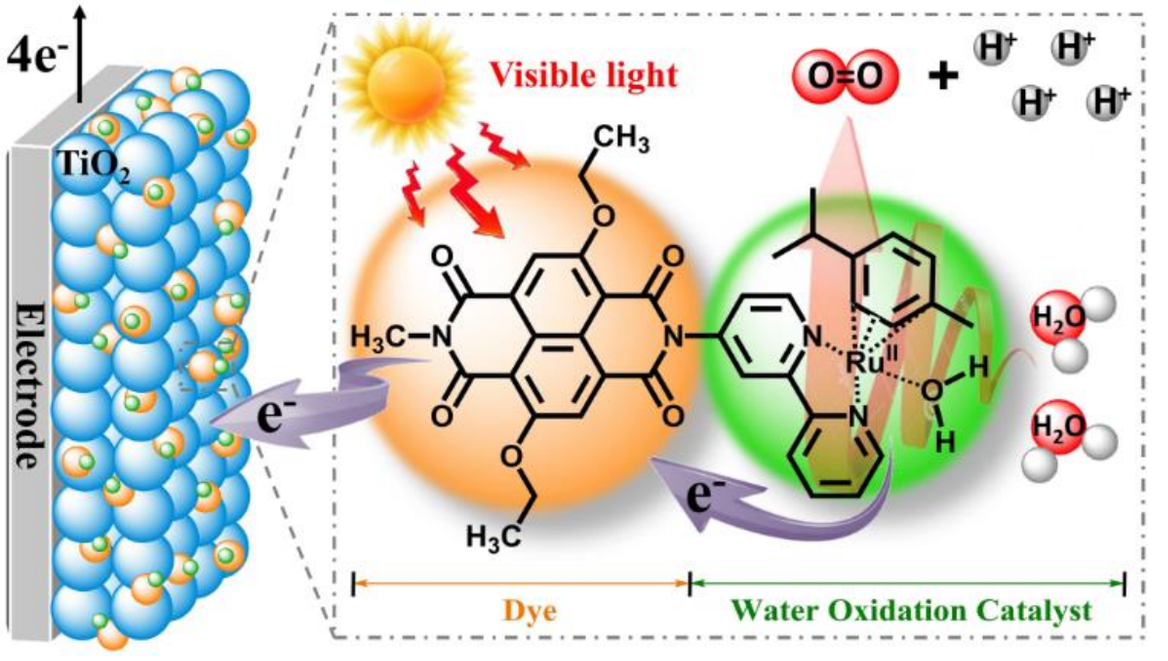

This chapter is based on:

Shao Yang, Jessica M. de Ruiter, Huub J.M. de Groot, and Francesco Buda, *The Journal of Physical Chemistry C*, **2019**, 123, 21403-21414, DOI: 10.1021/acs.jpcc.9b06401.

2

Abstract

The basic idea of a DS-PEC cell, inspired by natural photosynthesis, is to couple the photo-induced charge separation process to the catalytic water splitting. The photo-oxidized dye coupled to a WOC should exert a thermodynamic driving force for the catalytic cycle, while water provides the electrons for regenerating the oxidized dye. These conditions impose specific energetic constraints on the molecular components of the photoanode in the DS-PEC. Here we consider a supramolecular complex integrating a mononuclear Ru-based WOC with a fully organic NDI dye that is able to perform fast photo-induced electron injection into the conduction band of the titanium-dioxide semiconductor anode. By means of constrained AIMD simulations in explicit water solvent, it is shown that the oxidized NDI provides enough driving force for the whole photocatalytic water splitting cycle. The results provide strong evidence for the significant role of spin alignment and solvent rearrangement in facilitating the proton-coupled electron transfer processes. The predicted activation free energy barriers confirm that the O–O bond formation is the rate-limiting step. Our results expand the current understanding of the photocatalytic water oxidation mechanism and provide *ex-ante* computational guidelines for the optimization of high-performance DS-PEC devices.

2.1. Introduction

As the largest exploitable renewable energy source by far, solar energy has the potential to be an alternative to fossil fuel derived energy and to reduce environmental pollution.[1-2] The direct conversion of solar energy to storable chemical fuel is a promising strategy for providing a sustainable source of clean energy.[3-4] Inspired by natural photosynthesis and the successful photocatalytic water oxidation achieved in PSII, remarkable effort has been devoted to the development of efficient artificial photosynthesis devices for solar-to-fuel conversion.[5-12] A PEC cell performs this task by splitting water molecules into O_2, protons, and electrons at the anode, and evolving energy-rich H_2 or CO_2 derivatives at the cathode.[13-15] The water oxidation half-reaction is currently considered the most challenging and limiting step for the development of efficient PEC devices for the production of solar fuels.[16-18]

In the past decades, several systems have been proposed to facilitate the photocatalytic four-electron oxidation of water.[19-20] In a DS-PEC the photoanode combines visible light-absorbing photosensitizers for light harvesting and charge separation, and a WOC for water splitting.[21-25] The way these components are assembled will determine the efficiency and photostability of the device.[25] Much effort has been devoted to the exploration of assembling strategies: among others, the co-deposition method where the photosensitizer and the WOC are deposited as separate moieties on the semiconductor surface, and the supramolecular approach where the dye and WOC are covalently bound forming a complex anchored onto the semiconductor surface.[17,19] The performance of a dye-sensitized photoanode can be improved by a proper choice of the components in the WOC–dye supramolecular complex taking into account the energetics and light-absorbing properties of photosensitizers and WOCs.[26-32] It is also challenging to find an ideal dye that can absorb a significant region of the visible spectrum and have at the same time an appropriate redox potential to drive the whole catalytic water oxidation cycle coupled with an efficient WOC.[25] Computational studies constitute a very useful tool complementary to experiment by predicting reaction mechanisms and electronic properties of dye-sensitized photoanodes, thus avoiding an expensive trial and error strategy and providing a clear indication on the most cost effective direction to undertake.[33-38]

Scheme 2.1. Proposed photocatalytic water splitting cycle by Ru-based WOC–dye system, consisting of four catalytic steps.[a]

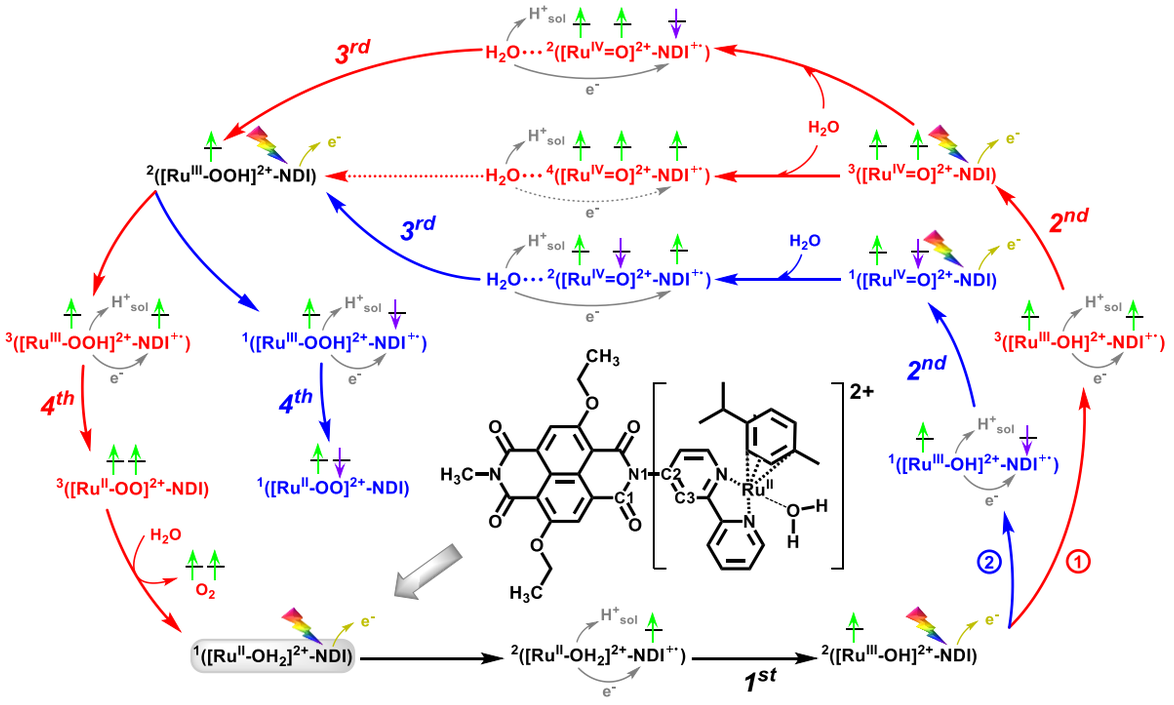

[a]The cycle starts from the $[(cy)Ru^{II}bpy(H_2O)]^{2+}$–NDI intermediate (indicated shortly as $^1([Ru^{II}–OH_2]^{2+}–NDI)$) on the bottom-left of the scheme. The $[Ru^{II}–OH_2]^{2+}$ motif can have singlet, triplet, or quintet spin multiplicity and it was calculated that the singlet multiplicity has the lower energy by 1 – 2 eV, which is due to the strong ligand field in the complex.[39] The schematic structure of this starting intermediate is shown explicitly in the inset. It is assumed that each light flash induces an electron injection (golden arrows) from the NDI to the semiconductor electrode or to the next stage in a tandem cell, leading to the photooxidation of NDI: NDI → $NDI^{+\bullet}$. Green (α electrons) and purple (β electrons) vertical arrows depict the spin of unpaired electrons located on the WOC and NDI. For each catalytic step we consider all possible spin alignments between unpaired electrons on the WOC and on the $NDI^{+\bullet}$, resulting in two alternative routes: ① in red and ② in blue. For the first step (in black), only the doublet state is possible. The dashed arrow indicates a process that is found to be thermodynamically unfavorable. H^+_{sol} represents the proton transferred to the solvent. The outer most pathway is most favorable according to the simulations. The superscript on the left indicates the spin multiplicity $2S+1$ for each intermediate.

We recently investigated *in silico* a supramolecular complex $[(cy)Ru^{II}bpy(H_2O)]^{2+}$–NDI (cy = *p*-cymene, bpy = 2,2′-bipyridine, NDI = 2,6-diethoxy-1,4,5,8-diimide-naphthalene; $^1([Ru^{II}–OH_2]^{2+}–NDI)$ in Scheme 2.1) anchored on a TiO_2 semiconductor surface.[40] The catalytic cycle of the mononuclear WOC $[(cy)Ru^{II}bpy(H_2O)]^{2+}$ has been systematically examined by means of a combination of theoretical and experimental techniques,[39] and

consists of four PCET steps.[41-44] The free energy change of this WOC for each catalytic step from the initial intermediate I_1 ($[Ru^{II}–OH_2]^{2+}$) to the final intermediate I_0 ($[Ru^{II}–OO]^{2+}$) is reported in Table A2.1 and Figure A2.1 in the Appendix.[39] The NDI chromophores family has shown good optical performance in photovoltaics, artificial photosystems, all-polymer solar cells, and potential in achieving photoinduced long-distance charge separation and reducing charge recombination.[45-50] In a recent computational work it has been shown that the NDI dye with diethoxy functional groups considered in this work (see Figure 2.1b) performs fast electron injection in the TiO_2 semiconductor conduction band on a ps time scale.[40] Furthermore, a very low activation barrier was estimated for the first water oxidation catalytic step upon photooxidation of the molecular photosensitizer ($NDI^{+\bullet}$) covalently bound to the Ru-based WOC.[40] The choice of anchoring groups with established chemical and thermal stabilities,[51-53] the inclusion of bridge units with rectifying properties,[54] and ancillary chromophores with complementary absorption properties and redox potentials[55] can contribute to the optimization of the photoanode design.

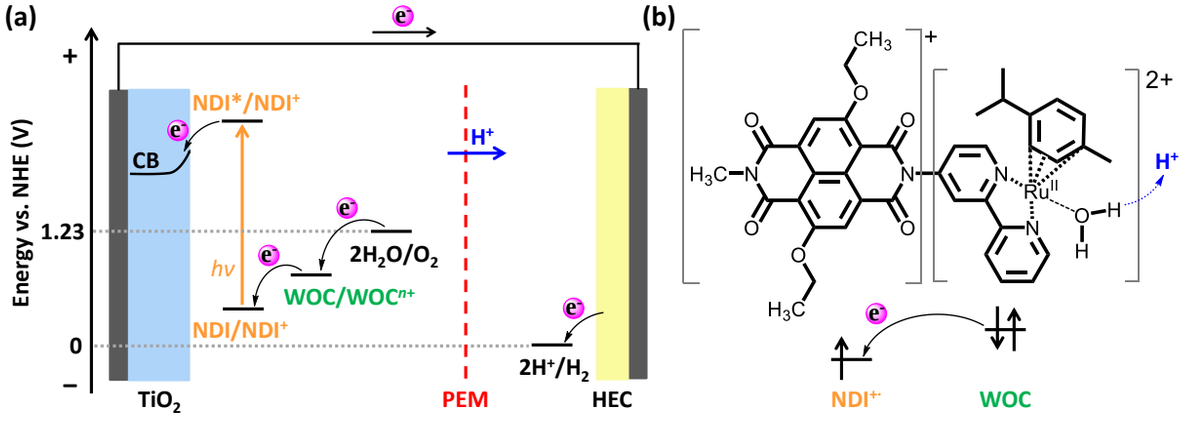

Figure 2.1. (a) Schematic diagram of a proposed DS-PEC for solar-energy conversion. PEM indicates a proton exchange membrane for selective proton transport to the HEC; (b) WOC–dye supramolecular complex considered in this work in the photooxidized state.

The role of the oxidized dye in this WOC–dye supramolecular complex is analogous to that of the redox-active tyrosine (Tyr-161) near the oxygen evolving complex in PSII, in stabilizing the hole and acting as primary electron acceptor during the catalytic water oxidation cycle.[8] In this work, we focus on the coupling between the catalyst and the dye and the ability of this photooxidized NDI dye to drive the whole water splitting cycle. By using static DFT calculations, we first

ascertain whether the NDI dye considered in this work has the basic energetic requirements, *i.e.*, enough oxidation power, to drive the whole catalytic cycle for water oxidation.[25] (see schematic energy diagram in Figures 2.1a). Moreover, by means of constrained AIMD simulations in explicit water solvent, we establish the free energy profile for all the catalytic reaction steps starting from the oxidized WOC–dye intermediates (see Scheme 2.1). This allows also to determine the activation energy ΔG^* that can be used to estimate the reaction rate. The effect of spin alignment between unpaired electrons on the WOC and on the $NDI^{+\bullet}$ is also explored (see route ① and ② in Scheme 2.1). In particular, for the second step starting from the oxidized WOC–dye intermediates $^1([Ru^{III}–OH]^{2+}–NDI^{+\bullet})$ (route ②) and $^3([Ru^{III}–OH]^{2+}–NDI^{+\bullet})$ (route ①) are considered, for the third step the intermediates $^2([Ru^{IV}=O]^{2+}–NDI^{+\bullet})$ and $^4([Ru^{IV}=O]^{2+}–NDI^{+\bullet})$, and for the fourth step the intermediates $^1([Ru^{III}–OOH]^{2+}–NDI^{+\bullet})$ and $^3([Ru^{III}–OOH]^{2+}–NDI^{+\bullet})$, respectively. A negative free energy change ΔG^0 is found for all the consecutive PCET steps, thus indicating that the oxidized $NDI^{+\bullet}$ is fit for purpose. The calculated activation free energy barriers ΔG^* show that the O–O bond formation is the rate-limiting step. The AIMD simulations clarify the coupling between the electron transfer process and the bond-breaking/-forming events.[56] Moreover, the explicit inclusion of the solvent highlights the active role of the water rearrangement in the PCET processes. The gained insight in the photocatalytic water oxidation mechanism provides guidelines for the design and optimization of efficient photoanodes for DS-PEC devices.

2.2 Computational Details

2.2.1 Geometry Optimization at DFT level

The initial geometry of all the catalytic intermediates of the WOC–dye supramolecular complex were optimized using DFT calculations employing the OPBE exchange-correlation functional[57] and the TZP basis set.[40] The OPBE functional has shown to be accurate in describing transition-metal complexes, including Ru-based WOCs.[58-63] In Table A2.2 we show a comparison between OPBE results and those obtained with the more commonly used PBE functional, which provides very similar results. In the geometry optimization, the continuum solvation model COSMO[64-65] for water was used. These static calculations are performed with the ADF software package.[66-67]

2.2.2 Constrained *ab initio* Molecular Dynamics

To obtain a realistic description of the catalytic reaction steps, the solvent was explicitly introduced in the simulations.[61, 68] An orthorhombic box of dimensions 25.1 × 17.7 × 14.4 Å^3 was used, containing the $[WOC]^{2+}$–dye solute and 162 water molecules. The explicitly solvated systems were investigated through AIMD for the singly oxidized form of the complex ($[WOC]^{2+}$–$dye^{+\bullet}$) using the CPMD program.[69] The solvent environment for the CPMD simulations (pure neutral water, no ion included) was generated using Discovery Studio 2.5.[70] Prior to the AIMD simulations, the solvent was equilibrated using the TIP3P model implemented in the CHARMM force field and CFF partial charge parameters at 300 K,[71] while the $[WOC]^{2+}$–dye complex was kept fixed. The volume was then adjusted using constant pressure (NPT simulations at atmospheric pressure for 0.2 ns), after which the system was further allowed to evolve with constant volume (NVT simulations for 2 ns).

A so-called regeneration step is carried out at the beginning of each PCET step by first removing the excess solvated proton from the simulation box and performing an unconstrained AIMD simulation of ~360 fs at room temperature to equilibrate the system. Subsequently, one electron is removed from the simulation box, and the oxidized state is further re-equilibrated for another ~360 fs at room temperature.

All the CPMD simulations were performed in an aqueous environment at 300 K, using GTH pseudopotentials for the ruthenium transition metal,[72] and DCACP pseudopotentials for the remaining atoms,[73] together with a plane wave cutoff of 70 Ry and the OPBE exchange-correlation functional. The water molecules are treated at the same DFT quantum-mechanical level as the solute, which is essential for the accurate description of the PCET steps following photoinduced electron injection from the NDI dye into the semiconductor. Periodic boundary conditions are applied with a time step of δt = 5 a.u. (1 a.u. = 0.0242 fs). Trajectory analysis and visualization for the CPMD output were carried out using VMD program.[74-75]

Scheme 2.2. The schematic structure of the hydroxide (a), oxo (b), and hydroperoxide ligand (c) with a nearby solvent water molecule.[a]

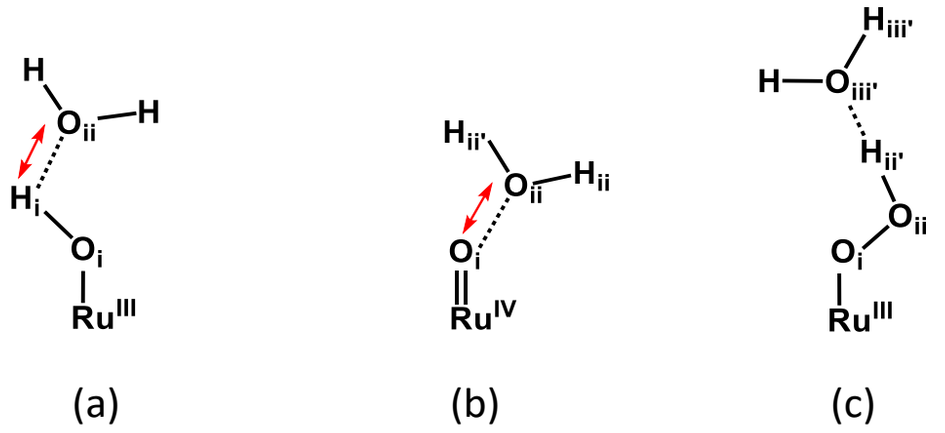

[a]The red double-sided arrow indicates the reaction coordinate considered for the (a) $[Ru^{III}–OH]^{2+}\cdots H_2O$ and (b) $[Ru^{IV}=O]^{2+}\cdots H_2O$ during the constrained MD simulations. The labeling of the atoms that are involved in the reaction steps is used throughout this paper.

Given that the catalytic reaction steps are unlikely to occur spontaneously during the typical AIMD simulation time scale, constrained MD and the so-called Blue Moon approach were employed as a rare event simulation technique.[76-78] The reaction coordinate (in this case the distance between two atoms shown in Scheme 2.2) is constrained to a series of fixed values along a reaction path for both route ① and ②:

(i) for the second PCET step (see Scheme 2.1), the distance between the proton (H_i) of the hydroxide ligand coordinated to the Ru atom and the oxygen (O_{ii}) of one solvent water molecule in the vicinity of $^2([Ru^{III}–OH]^{2+})$ is constrained in the range 1.6 – 1.0 Å (see Scheme 2.2a);

(ii) for the third PCET step, the distance between the oxygen (O_i) coordinated to the Ru atom and the oxygen (O_{ii}) of one solvent water molecule is constrained in the range 3.0 – 1.5 Å (see Scheme 2.2b);

(iii) for the fourth PCET step, no constraint is applied in the simulations (see Scheme 2.2c).

For each value of the reaction coordinate a time-averaged constraint force $\langle\lambda\rangle$ is obtained. This time-averaged constraint force is equal to zero at an equilibrium or transition state. The free energy change for each catalytic step is then obtained by thermodynamic integration along the reaction path.[56, 79-81]

2.3. Results and Discussion

The whole photocatalytic water splitting cycle via both route ① and ②, as depicted in Scheme 2.1, is explored with AIMD simulations in explicit water solvent. In previous work we have shown that, when excited with visible light, the NDI is able to inject an electron into a TiO_2 semiconductor surface on a time scale of ~1 ps.[40] Therefore we assume that at the beginning of the simulation for each catalytic step, the system is already in its oxidized form: $[WOC]^{2+}$–$dye^{+\bullet}$.

Table 2.1. Computed activation free energy barrier ΔG^* (in kcal mol^{-1}), thermodynamic driving force ΔG^o (in kcal mol^{-1}), and estimated reaction rate k (in s^{-1}) for the four redox couples along the whole catalytic cycle and different spin alignments along the routes ① and ② shown in Scheme 2.1.[a]

Step	Route	$2S+1$	Initial state	Final state	ΔG^*	ΔG^o	k
1st			$[Ru^{II}–OH_2]^{2+}$–$NDI^{+\bullet}$	$[Ru^{III}–OH]^{2+}$–NDI + H^+_{sol}			
	①+②	2	↑	↑	1.7	−4.0	3.6×10^{11}
2nd			$[Ru^{III}–OH]^{2+}$–$NDI^{+\bullet}$	$[Ru^{IV}=O]^{2+}$–NDI + H^+_{sol}			
	①	3	↑ ↑	↑ ↑	2.3	−10.7	1.3×10^{11}
	②	1	↑ ↓	↑ ↓	4.6	−1.1	2.8×10^{9}
3rd			$[Ru^{IV}=O]^{2+}$–$NDI^{+\bullet}$ + H_2O_{sol}	$[Ru^{III}–OOH]^{2+}$–NDI + H^+_{sol}			
	①	2	↑ ↑ ↓	↑	15.9	−8.5	15.7
		4	↑ ↑ ↑				
	②	2	↑ ↓ ↑	↑	9.0	−17.1	1.7×10^{6}
4th			$[Ru^{III}–OOH]^{2+}$–$NDI^{+\bullet}$	$[Ru^{II}–OO]^{2+}$–NDI + H^+_{sol}			
	①+②	1	↑ ↓				
		3	↑ ↑	↑ ↑			

[a]For each intermediate it is indicated explicitly where the unpaired electrons are localized, on the Ru-based catalyst or on the NDI (↑ for the α electron and ↓ for the β electron). $2S+1$ is the spin multiplicity of the system. H^+_{sol} and H_2O_{sol} represent the solvated proton and a solvent water molecule, respectively. For the 3rd step the $S = 3/2$ state turns out to be thermodynamically unfavorable compared to the $S = 1/2$ configuration in route ①. The 4th step is found to proceed spontaneously at room temperature for both spin states, which implies no significant activation barrier. The results for the first step are from reference 40.

Before starting the AIMD simulations, we have checked with static DFT calculations whether the SOMO on the oxidized dye is lower in energy than the HOMO localized on the catalyst, since this is a basic energetic requirement to allow for electron transfer from the WOC to the dye, thus regenerating the

ground state of the dye for the next photoinduced catalytic step (see Figure 2.1). It is found that this energy level alignment is indeed satisfied for all the intermediates in the catalytic cycle following route ①, which turned out to be the most favorable route: The orbital energy difference is in the range ~0.1 – 0.3 eV (see Figure A2.2 and Table A2.2 in appendix).

Table 2.1 summarizes the computed activation free energy barrier ΔG^*, the free energy change from the initial to the final state (thermodynamic driving force ΔG^0), and estimated reaction rate k for the whole catalytic cycle and different spin alignments shown in Scheme 2.1. In the following we discuss in detail the most favorable catalytic cycle, while results concerning thermodynamically unfavorable catalytic steps are reported in the appendix for comparison.

We have previously shown that the first PCET catalytic step ($[Ru^{II}–OH_2]^{2+}–NDI^{+\bullet} \rightarrow [Ru^{III}–OH]^{2+}–NDI + H^+_{sol}$) is exothermic with a thermodynamic driving force $\Delta G^0 \approx -4$ kcal mol^{-1} (~0.17 eV) and presents a very low activation free energy barrier $\Delta G^* \approx 1.7$ kcal mol^{-1} (~0.074 eV), which is only ~3 $k_B T$ at room temperature, corresponding with a very fast rate (see Table 2.1).[40] In the following sections the successive PCET catalytic water oxidation steps are discussed.

2.3.1 Second Catalytic Water Oxidation Step

The system with the oxidized intermediate $^3([Ru^{III}–OH]^{2+}–NDI^{+\bullet})$ in the $S = 1$ state (see route ① in Scheme 2.1) is equilibrated at room temperature without constraint for ~2 ps (see Figure 2.2). By tracing the spin density along the free MD simulation trajectory we observe the photoinduced hole localized on the oxidized $NDI^{+\bullet}$ and one unpaired electron localized on the catalyst as expected (see Figure 2.2, inset). The analysis of the MD trajectory shows the hydroxide ligand forming a strong hydrogen bond with a nearby water molecule with an average distance $d(H_i–O_{ii})$ of ~1.7 Å (see Figure 2.2). Although we can observe some spontaneous attempts of proton transfer from the hydroxide to the neighboring water molecule, this process may occur on a time scale that is still prohibitive for AIMD.[40] Thus we use constrained AIMD to analyze the second PCET step shown in eq. 2.1, where H^+_{sol} represents the solvated proton:

$$^3([Ru^{III}–OH]^{2+}–NDI^{+\bullet}) \leftrightarrow {}^3([Ru^{IV}=O]^{2+}–NDI) + H^+_{sol} \qquad (2.1)$$

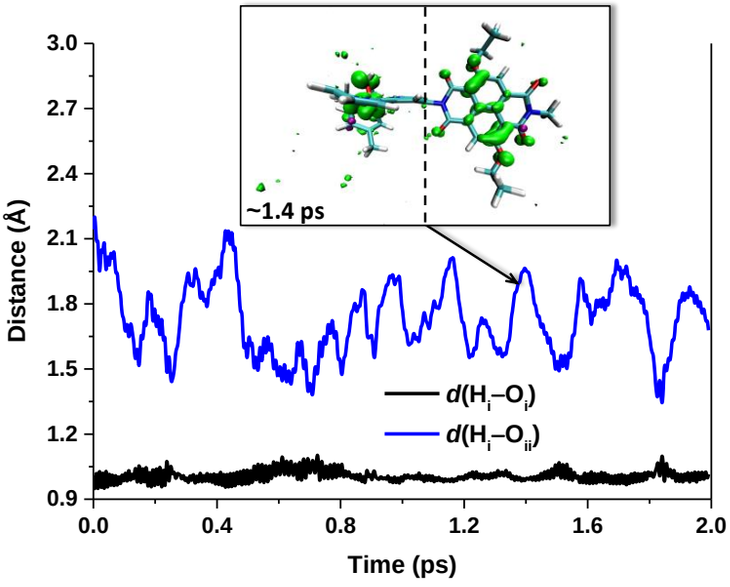

Figure 2.2. Time evolution of the geometrical parameter $d(H_i–O_i)$ (black line) and $d(H_i–O_{ii})$ (blue line) along the free MD simulation trajectory for the oxidized intermediate $^3([Ru^{III}–OH]^{2+}–NDI^{+\bullet})$ in route ①. See scheme 2.2 for the atomic labelling. We can observe a shortened $d(H_i–O_{ii}) \approx 1.3$ Å and a corresponding stretched $d(H_i–O_i) \approx 1.1$ Å at several time intervals (~0.25 ps, ~0.71 ps, and ~1.84 ps), which can be interpreted as spontaneous attempts of proton transfer from the hydroxide to the neighboring water molecule. The inset shows the spin density isosurface (green) computed at a snapshot taken at ~1.4 ps, clearly indicating that one unpaired α electron is localized on the catalyst and the other unpaired α electron on the oxidized $NDI^{+\bullet}$.

Given the average $d(H_i–O_{ii})$ of ~1.7 Å extracted from the unconstrained MD simulation, a series of constrained MD simulations are performed with $d(H_i \leftarrow O_{ii})$ as the reaction coordinate (see Scheme 2.2), which is shortened gradually from 1.6 Å to 1.05 Å (noted in grey in Figure 2.3), to estimate the free energy profile along the reaction path. To test the stability of the obtained intermediate $^3([Ru^{IV}=O]^{2+}–NDI)$ in the catalytic cycle, we also perform a free MD run at the end, following the 1.05 Å constrained simulation. The variation of the total spin density localized on the catalyst (black line), the time evolution of the geometrical parameter $d(H_i–O_i)$ (magenta line), and the distance between Ru and H_3O^+ along different constrained MD trajectories are collected in Figure 2.3, top, middle and bottom, respectively.

For the first two MD trajectories with constrained distances 1.6 and 1.4 Å, one unpaired electron is localized on the oxidized $NDI^{+\bullet}$ dye and the other unpaired electron on the catalyst (see Figure 2.3, inset a). The spin density initially localized on the oxidized $NDI^{+\bullet}$ gradually moves to the catalyst as a result of the shortening

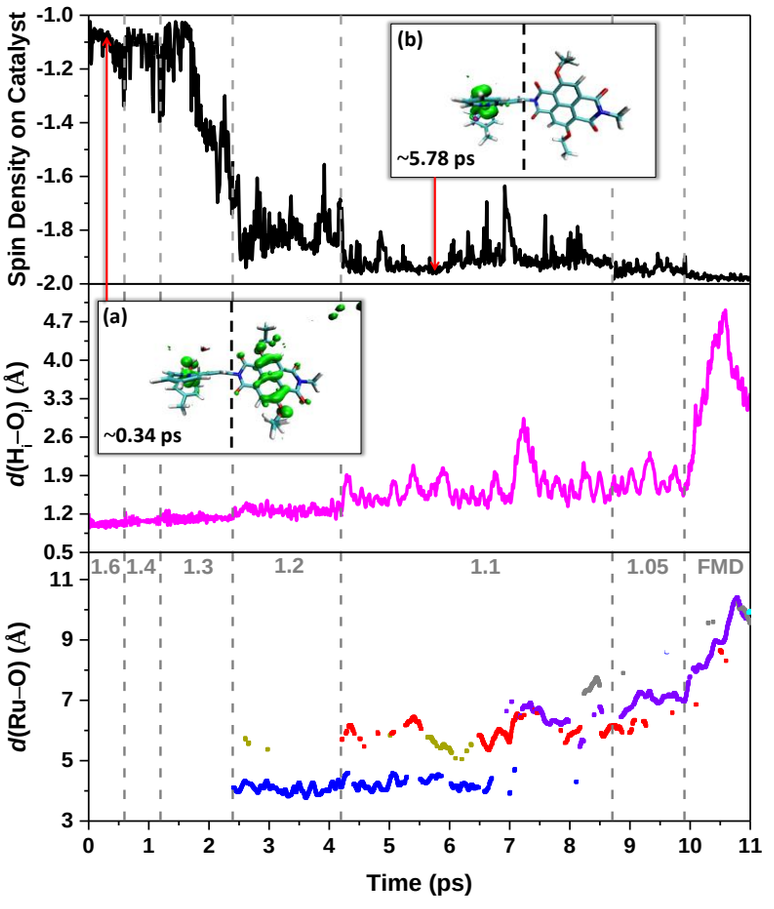

Figure 2.3. (top panel) The spin density integrated over the half of the simulation box including the catalyst (left-hand side of the dashed black line in the inset a and b) along the MD trajectories starting from the oxidized intermediate $^3([Ru^{III}–OH]^{2+}–NDI^{+\bullet})$ (see route ① in Scheme 2.1). An integrated spin density value of –1 corresponds to one unpaired α electron. The starting configuration at $d(H_i \leftarrow O_{ii})$ = 1.6 Å (see Scheme 2.2 for the atomic labels) has been extracted from a previous unconstrained simulation of the first catalytic intermediate. (middle panel) Time evolution of the geometrical parameter $d(H_i–O_i)$ (see Scheme 2.2) along the constrained and free MD (FMD) trajectory. (bottom panel) The distance between Ru and H_3O^+, defined as an oxygen atom with 3 H within a radius of 1.2 Å, illustrating the proton diffusion during the MD simulations. The analysis of the trajectories shows that only one oxygen is in the H_3O^+ form at any time, and the excess proton associates primarily to four different oxygens (indicated with different colours: blue, gold, red and purple) during the simulation. The value of the constrained reaction coordinate $d(H_i \leftarrow O_{ii})$ applied in the MD simulations is noted in grey. Inset (a) shows a snapshot from the beginning of the trajectory corresponding to a constraint value of 1.6 Å, where one unpaired α electron (green spin density isosurface) is localized on the catalyst and the other unpaired α electron on the $NDI^{+\bullet}$; Inset (b) shows a snapshot from the trajectory corresponding to a constraint value of 1.1 Å, where two unpaired α electrons are both localized on the catalyst.

of $d(H_i \leftarrow O_{ii})$ and corresponding weakening of the $H_i–O_i$ bond (see Figure 2.3, top and middle). When $d(H_i \leftarrow O_{ii})$ = 1.2 Å the H_i proton is shared between the

hydroxide and the attacking water molecule with an average $d(H_i–O_i)$ of ~1.2 Å, leading to the formation of the first H_3O^+ (see Figure 2.3, bottom). Further shortening of $d(H_i \leftarrow O_{ii})$ to 1.1 Å induces full transfer of an electron from the catalyst to the oxidized $NDI^{+\bullet}$ dye. This results in filling the hole on the $NDI^{+\bullet}$ as shown in Figure 2.3, inset b, where no spin density is localized on the NDI. During the same constrained MD at 1.1 Å we observe that the $H_i–O_i$ bond is totally broken and the generated proton diffuses from O_{ii} of the attacking water molecule to neighboring water molecules (see Figure 2.3, bottom). At the end of the constrained MD simulation, the Ru catalyst has two unpaired α electrons as expected on the basis of previous calculations indicating that the $[Ru^{IV}=O]^{2+}$ intermediate has a triplet ground-state (S = 1).[39] The obtained product $^3([Ru^{IV}=O]^{2+}–NDI)$ is verified to be stable at room temperature during the free MD simulation (FMD in Figure 2.3) as no proton or electron recombination is observed and the released proton diffuses through the solvent. The proton diffusion process in liquid water can be described by the Grotthuss mechanism involving covalent bond breaking and formation within the hydrogen-bonding network.[82-89]

The free energy profile along the reaction coordinate $d(H_i \leftarrow O_{ii})$ is estimated by numerical integration of the mean forces extracted from the constrained dynamics,[56, 81] and is reported in Figure 2.4 (bottom). The mean force values corresponding to the applied constraints are presented in Figure 2.4 (top) together with the 100-point Akima spline interpolation utilized for the integration. In Figures A2.3 and A2.4, we show that the running average of the Lagrangian multiplier reaches a stable value even within a relatively short MD timescale of ~0.5 ps. The second catalytic step shows an activation energy barrier $\Delta G^* \approx 2.3$ kcal mol^{-1} (~0.10 eV) slightly higher than in the first catalytic step (see Table 2.1). Noticeably, a much larger driving force $\Delta G^o \approx -10.7$ kcal mol^{-1} (~0.46 eV) is found for this step compared to the first, indicating an exothermic process after the photooxidation and a quite stable product intermediate $^3([Ru^{IV}=O]^{2+}–NDI)$ in the S = 1 state. The $Ru–O_i$ bond is shortened from an average length of 1.93 Å to 1.76 Å through this reaction, extracted from the unconstrained MD simulation before and after the second catalytic step, which contributes to the stabilization of the obtained intermediate. These findings demonstrate that the second catalytic water oxidation step in route ① is thermodynamically

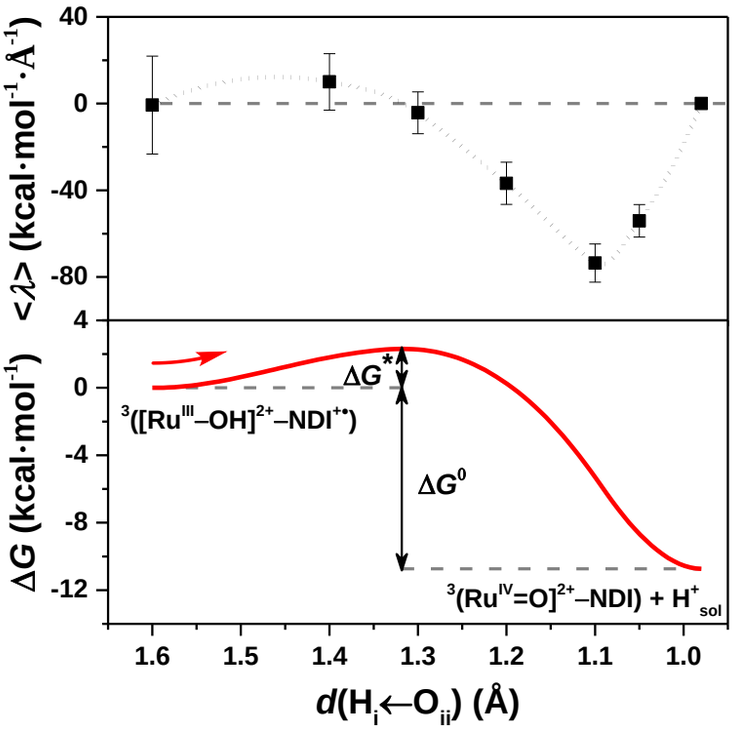

Figure 2.4. (top panel) The constraint mean force represented by the Lagrangian multiplier $\langle\lambda\rangle$ (black squares) computed for each constrained MD simulation as a function of the reaction coordinate $d(H_i \leftarrow O_{ii})$ along route ① for the triplet spin state. The mean force at the equilibrium distance $d(H_i–O_{ii})$ = 0.98 Å evaluated in the FMD has been set to 0. The 100-point Akima spline interpolation (dotted line) is used to interpolate the mean forces including also the zero point at equilibrium. The error bars indicate the standard deviations. (bottom panel) Free energy profile along the reaction coordinate $d(H_i \leftarrow O_{ii})$ computed from thermodynamic integration of the interpolated time-averaged mean forces. The initial and final intermediates are also indicated.

favorable upon photooxidation of the dye and can indeed proceed at a high rate at room temperature given the low activation energy, similar to the first catalytic step (see Table 2.1).

The opposite spin orientation on NDI has been also investigated and the results are reported in Figures A2.5 – A2.7 and Table A2.3. The initial free MD equilibration for the oxidized intermediate $^1([Ru^{III}–OH]^{2+}–NDI^{+\bullet})$, in the S = 0 state, clearly shows the antiparallel spins (see inset b in Figure A2.7). Considering the relatively higher activation energy barrier and smaller driving force along route ② compared to that of route ① (see Table 2.1 and Figure A2.5), route ② is thermodynamically less favourable. Moreover, the product intermediate $^3([Ru^{IV}=O]^{2+}–NDI)$ is found to be more stable than $^1([Ru^{IV}=O]^{2+}–NDI)$ (see Figure A2.6 and Table A2.3), confirming that route ① is most likely for this catalytic step.

2.3.2 Third Catalytic Water Oxidation Step: O–O Bond Formation

The third catalytic step involves the O–O bond formation and is commonly found to be the most thermodynamically demanding process in catalytic water oxidation (see also Table A2.1 and Figure A2.1).[34, 39, 90] To check whether the selected NDI dye is able to drive the third catalytic water oxidation step, AIMD simulations are performed for the oxidized complex $[Ru^{IV}{=}O]^{2+}$–$NDI^{+\bullet}$ in explicit water solvent.

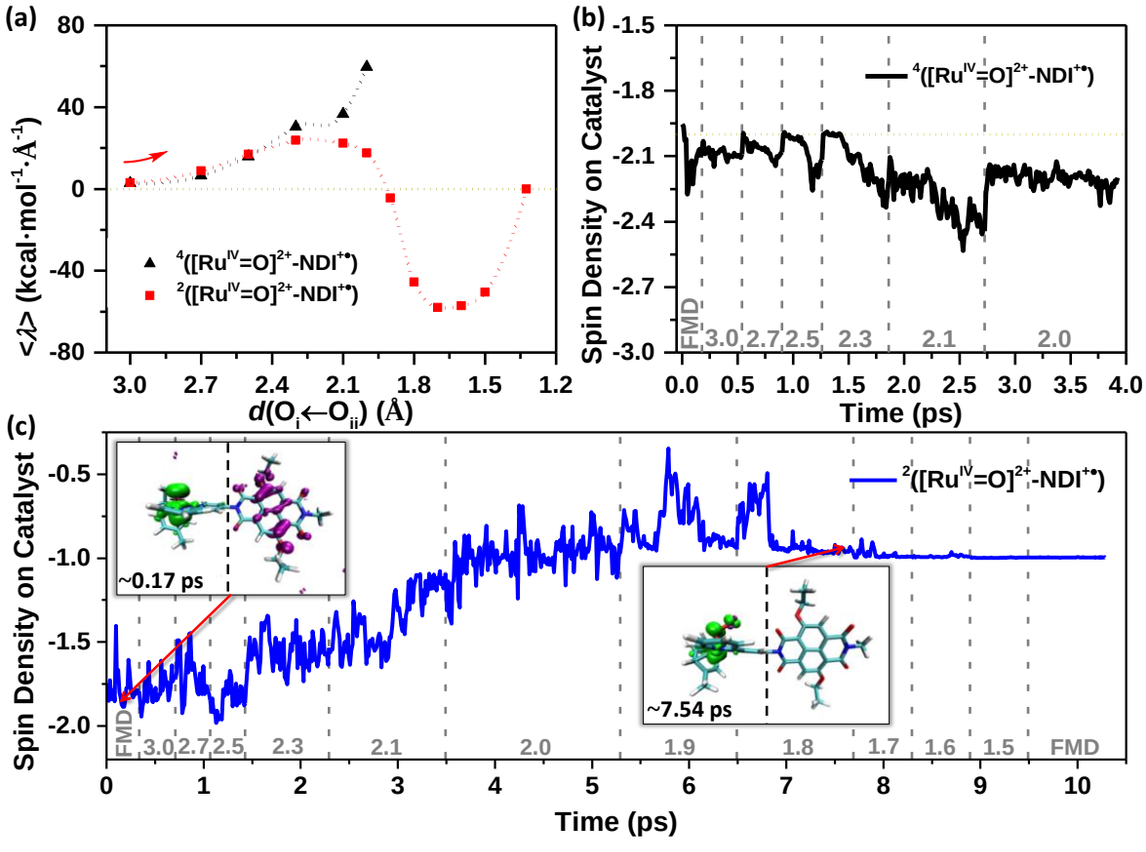

Figure 2.5. (a) Average constraint force represented by the Lagrangian multiplier $\langle\lambda\rangle$ computed for each constrained MD simulation with quartet multiplicity (black triangles) and doublet multiplicity (red squares) as a function of the reaction coordinate $d(O_i{\leftarrow}O_{ii})$. The Akima spline (100 points) is used to interpolate the mean forces (dotted lines). The point at $d(O_i{-}O_{ii})$ = 1.32 Å corresponds to the equilibrium product state and thus its $\langle\lambda\rangle$ is assumed to be zero. The spin density integrated over the half of the simulation box that includes the catalyst along the constrained and free MD trajectories is shown in (b) for the quartet and in (c) for the doublet state. In the panels (b) and (c) the value of the constrained reaction coordinate $d(O_i{\leftarrow}O_{ii})$ in the MD simulations is also indicated in grey. Inset (left) shows a snapshot from the FMD trajectory, where two unpaired α electrons (green spin density isosurface) are localized on the catalyst and one unpaired β electron (purple spin density isosurface) on the oxidized $NDI^{+\bullet}$; Inset (right) shows a snapshot from the final part of the trajectory corresponding to a constraint value of 1.8 Å, where only one unpaired α electron is left on the catalyst.

In the $[Ru^{IV}=O]^{2+}$–$NDI^{+\bullet}$ intermediate there are two unpaired electrons localized on the catalyst and one unpaired electron on the oxidized dye. Two specific initial spin states are therefore investigated (see route ① in Scheme 2.1 and Table 2.1):

(I) $^4([Ru^{IV}=O]^{2+}–NDI^{+\bullet})$ (S = 3/2): two unpaired α electrons (↑) localized on the catalyst and one unpaired α electron localized on the oxidized $NDI^{+\bullet}$ dye;

(II) $^2([Ru^{IV}=O]^{2+}–NDI^{+\bullet})$ (S = 1/2): two unpaired α electrons localized on the catalyst and one unpaired β electron (with opposite spin ↓) localized on the oxidized $NDI^{+\bullet}$ dye.

We perform constrained MD simulations for both spin states. The results show that the calculated time-averaged constraint force $\langle\lambda\rangle$ obtained in the quartet multiplicity case (I) increases systematically (see black triangles in Figure 2.5a) and no electron transfer from the catalyst to the oxidized $NDI^{+\bullet}$ occurs (see Figure 2.5b) when shortening the constraint distance $d(O_i \leftarrow O_{ii})$ (see Scheme 2.2b). This implies that the O–O bond formation is thermodynamically unfavorable for this spin alignment. Instead, the doublet state (II) facilitates the formation of this bond in the third catalytic step (see eq. 2.2, where H_2O_{sol} represents the solvated attacking water molecule), demonstrating again the significant role of spin alignment in the investigated supramolecular complex.[91-93] In the following we then focus only on the S = 1/2 spin state for the third redox couple.

$$^2([Ru^{IV}=O]^{2+}–NDI^{+\bullet}) + H_2O_{sol} \quad \leftrightarrow \quad ^2([Ru^{III}–OOH]^{2+}–NDI) + H^+_{sol} \qquad (2.2)$$

The spin density for the reactant (doublet) in route ① (see eq. 2.2) shows as expected two unpaired electrons localized on the catalyst and one unpaired electron localized on the oxidized $NDI^{+\bullet}$ with antiparallel spin. (see Figure 2.5c, inset (left)).

According to the results of our AIMD simulations, the third catalytic water oxidation step can be described by three features: (1) attacking water rearrangement to reach a favorable orientation with respect to the oxygen ligand; (2) electron transfer from the WOC to the photoinduced hole on the oxidized $NDI^{+\bullet}$; (3) proton transfer and diffusion into the solvent bulk.

2.3.2.1 Attacking Water Rearrangement and Electron Transfer

After equilibration of the system during the free MD simulation, one water molecule in the vicinity of the $^3([Ru^{IV}=O]^{2+})$ group is selected as the attacking water molecule during the constrained MD trajectories (see Figure 2.6a). A few representative configurations with constrained $d(O_i \leftarrow O_{ii})$ values ranging from 3.0 to 2.1 Å are shown in Figure 2.6(b–f).

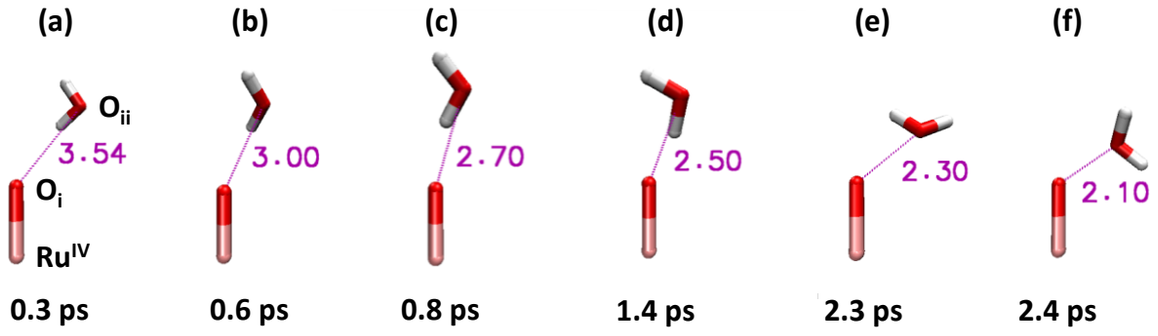

Figure 2.6. (a) Configuration of the attacking water molecule during the FMD at room temperature. (b) – (f) Snapshots from the constrained MD trajectories at different $d(O_i \leftarrow O_{ii})$ (in purple) with spin multiplicity $2S+1 = 2$. Only the attacking water molecule, the ruthenium metal center and the oxygen coordinating to it are shown explicitly. The orientation rearrangement of the attacking water molecule during this process is clearly visible.

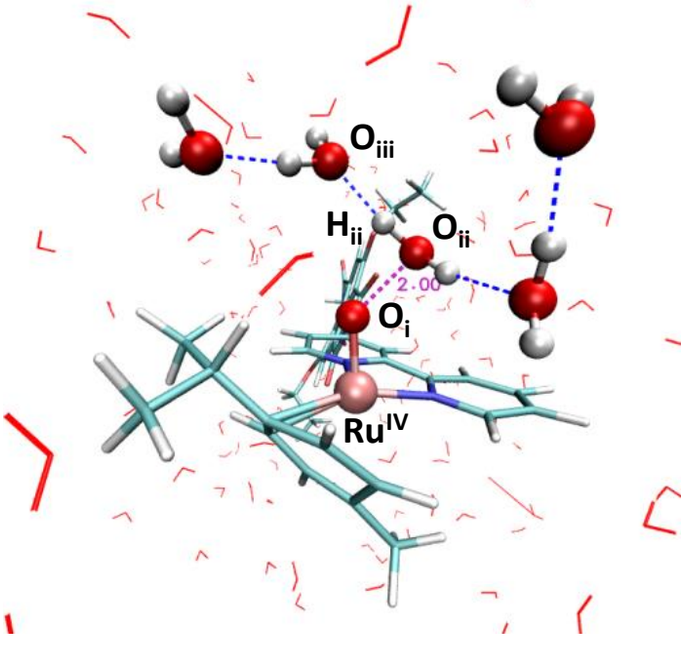

Figure 2.7. The attacking water molecule and the neighboring water molecules along the hydrogen-bonding network (dashed blue lines) at the beginning of the constrained simulation with $d(O_i \leftarrow O_{ii})$ = 2.0 Å.

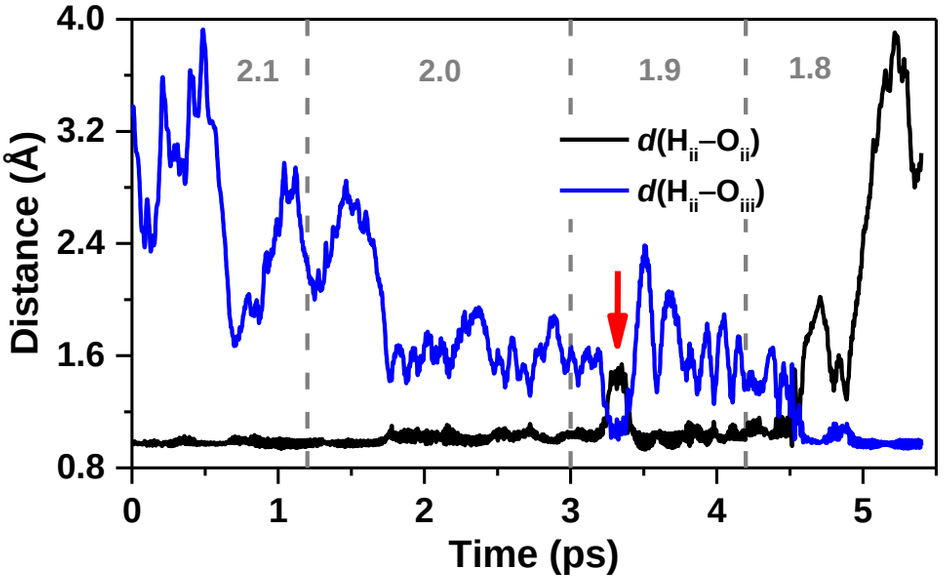

Figure 2.8. Time evolution of the geometrical parameter $d(H_{ii}–O_{ii})$ (black line) and $d(H_{ii}–O_{iii})$ (blue line) along the constrained MD simulations (route ①). See **Figure 2.7** for the atomic labels. The value of the constrained reaction coordinate $d(O_i \leftarrow O_{ii})$ in the MD simulations is noted in grey. The red vertical arrow indicates a first proton transfer attempt during the constrained 1.9 Å simulation followed by fast back reaction.

The attacking water molecule has initially one hydrogen atom pointing to the oxygen ligand (O_i) of the $^3([Ru^{IV}{=}O]^{2+})$ center (2.5 Å < $d(O_i \leftarrow O_{ii})$ < 3.0 Å). When the constrained $d(O_i \leftarrow O_{ii})$ is shortened to 2.3 Å, the attacking water molecule starts to rotate and reaches a state with its oxygen atom (O_{ii}) now pointing towards the oxygen ligand (O_i), preparing for the O–O bond formation. Moreover, the attacking water molecule forms strong hydrogen bonds with neighboring water molecules at the beginning of the 2.0 Å simulation (see Figure 2.7). This hydrogen bonding network not only stabilizes the configuration of the attacking water molecule but also predisposes the system for the subsequent proton diffusion process.

The integrated spin density localized on the catalyst along the constrained MD trajectories is reported in Figure 2.5c to clarify the electron dynamics during this catalytic step. During the initial water attack stage (2.5 Å < $d(O_i \leftarrow O_{ii})$ < 3.0 Å), the spin density localized on the catalyst fluctuates around an average value of ~–1.8, corresponding to the expected triplet state of this catalyst intermediate, while one unpaired electron with antiparallel spin is localized on the oxidized $NDI^{+\bullet}$ (see Figure 2.5c, inset (left)). The shortening of $d(O_i \leftarrow O_{ii})$ from 2.5 Å to 2.0 Å induces the electron transfer from the catalyst to the oxidized $NDI^{+\bullet}$ dye, which

is facilitated by the rearrangement of the attacking water. The spin density localized on the catalyst during the constrained 2.0 Å simulation fluctuates around an average of –1, indicating the accomplishment of the electron transfer and the filling of the photoinduced hole on the $NDI^{+\bullet}$ dye. No proton transfer occurs during the constrained 2.0 Å dynamics, even though the electron transfer has already taken place. The H_{ii}–O_{ii} bond (see Scheme 2.2b) is however slightly weakened with a maximum distance ~1.1 Å (see Figure 2.8). When we further shorten the constrained $d(O_i \leftarrow O_{ii})$ from 1.9 to 1.5 Å, the proton transfer takes place (see next section) and the spin density on the catalyst reaches a stable value of –1, indicating only one unpaired electron finally left on the catalyst (see Figure 2.5c, inset (right)) and no back reaction occurs even when the constraint is released (FMD).

2.3.2.2 Proton Diffusion

The time evolution of the $d(H_{ii}–O_{ii})$ and $d(H_{ii}–O_{iii})$ (see Figure 2.9b, top) shows that the H_{ii} proton does several attempts between 6.7 ps and 6.9 ps before eventually jumping from oxygen O_{ii} to O_{iii}. Almost simultaneously to the H_{ii} proton transfer from O_{ii} to O_{iii}, the H_{iii} proton makes a first spontaneous jump from oxygen O_{iii} to O_{iv}, as the acceptance of the H_{ii} proton by the oxygen O_{iii} weakens the H_{iii}–O_{iii} bond (see Figure 2.9b, middle, ~6.85 ps). The H_{iii} proton appears to be shared by the oxygen O_{iii} and O_{iv}, until it is fully transferred to O_{iv} (see Figure 2.9b, middle, ~7.2 ps). Soon after, the H_{iv} proton is successfully transferred from O_{iv} to O_v (see Figure 2.9b, bottom, ~7.4 ps). These results provide strong evidence that the nature of this proton diffusion process is well described by the Grotthuss mechanism.[82-85] The excess proton diffuses further into the solvent bulk during the following constrained MD simulations with fixed $d(O_i \leftarrow O_{ii})$ from 1.7 to 1.5 Å. More importantly, no backward proton transfer is observed even after removing the constraint at the end of 1.5 Å simulation, showing the stability of the newly formed hydroperoxo intermediate $^2([Ru^{III}–OOH]^{2+}–NDI)$ in the S = 1/2 state. For the FMD trajectory the $d(O_i–O_{ii})$ fluctuates around its average of 1.32 Å, indicating the formation of a strong O–O bond after the proton diffusion process. For comparison, the O–O bond length in molecular hydrogen peroxide is 1.47 Å.[56] The relatively short O–O bond can be further ascribed to the weakened O_{ii}–$H_{ii'}$ bond (see Figure 2.9a), which will be discussed in detail in the next section.

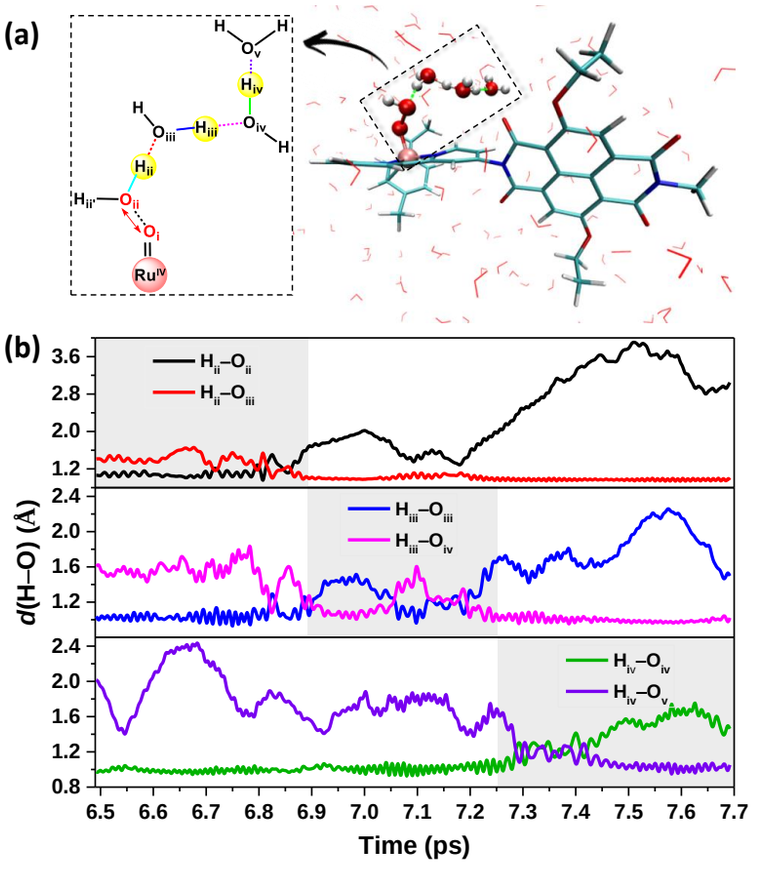

Figure 2.9. (a) Water molecules involved in the proton diffusion path from oxygen O_{ii} into the solvent bulk. (b) Time evolution of the d(H–O) distances contributing to the proton diffusion along the constrained MD trajectory corresponding to the constraint value $d(O_i \leftarrow O_{ii})$ = 1.8 Å. The time range is consistent with Figure 2.5c.

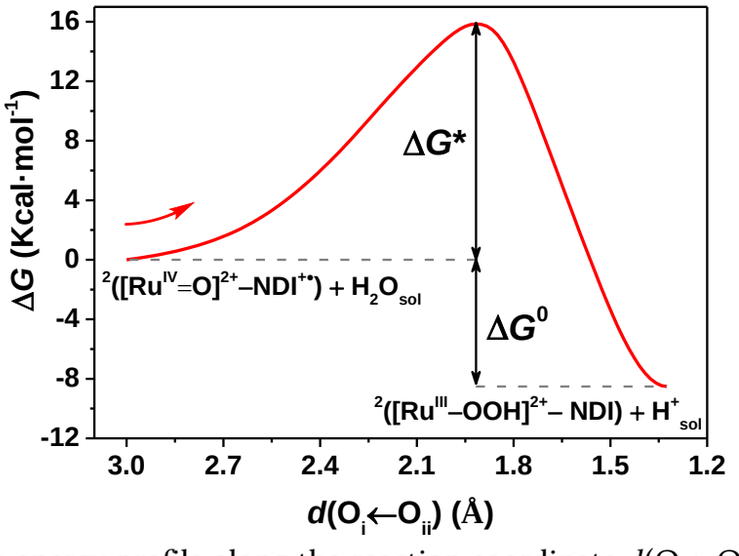

Figure 2.10. Free energy profile along the reaction coordinate $d(O_i \leftarrow O_{ii})$ computed by thermodynamic integration. All the constrained MD simulations are performed with doublet multiplicity, corresponding to having two unpaired α electrons on the Ru-based catalyst and one β electron on the oxidized $NDI^{+\bullet}$. The initial and final intermediates are also indicated.

The time-averaged mean forces associated with the applied constraint are collected in Figure 2.5a (red squares), leading to the free energy profile shown in Figure 2.10 by thermodynamic integration. Well in line with the O–O bond formation representing the rate-limiting step, it presents a considerably higher activation energy barrier $\Delta G^* \approx 15.9$ kcal mol^{-1} (~0.69 eV) compared to the previous two catalytic steps (see Table 2.1). This step is indeed normally considered as the thermodynamic bottleneck of the water splitting process in mononuclear WOC.[21] In addition to the involvement of the O–O bond formation, such a high reaction barrier can be partly attributed to the low-energy starting point, since the second intermediate ^{3}([Ru^{IV}=O]$^{2+}$–NDI) is quite stable in the water solvent.[39] However, also this catalytic step leading to the intermediate ^{2}([Ru^{III}–OOH]$^{2+}$–NDI) is found to be exothermic after photooxidation with a predicted driving force $\Delta G^\circ \approx -8.5$ kcal mol^{-1} (~0.37 eV) (Figure 2.10). In spite of the considerably high activation energy barrier, the oxidized NDI$^{+\bullet}$ dye is still capable of driving the formation of the O–O bond, provided that antiparallel spin alignment is achieved. According to transition state theory[94-97], the reaction rate k is determined by the activation free energy barrier ΔG^* according to

$$k = \frac{k_B T}{h} \cdot e^{-\frac{\Delta G^*}{RT}}. \qquad (2.3)$$

The calculated rates of the first three catalytic steps along route ① (as well as route ②, for comparison) are listed in Table 2.1. The first two catalytic steps are very fast with a rate of k = ~3.6×10^{11} s^{-1} and k = ~1.3×10^{11} s^{-1} respectively, while the third step is around ten orders of magnitude slower. Although the third step involving the O–O bond formation with a rate of k = ~15.7 s^{-1} is unquestionably the rate-limiting step, the specific WOC coupled to the NDI dye shows a competitive rate compared to some characteristic Ru-based mononuclear WOCs.[21] Due to the slow rate of this step, electron recombination from the semiconductor to the NDI might compete with the electron transfer from the WOC to the dye, therefore reducing the efficiency of the whole process.[98-99]

Additionally, the third step along route ② (see Scheme 2.1) has been also investigated and the results are reported in Figure 2.11. The computed free energy profile shows that this route is thermodynamically viable, leading to the same product intermediate ^{2}([Ru^{III}–OOH]$^{2+}$–NDI) in the S = 1/2 state as for route ①

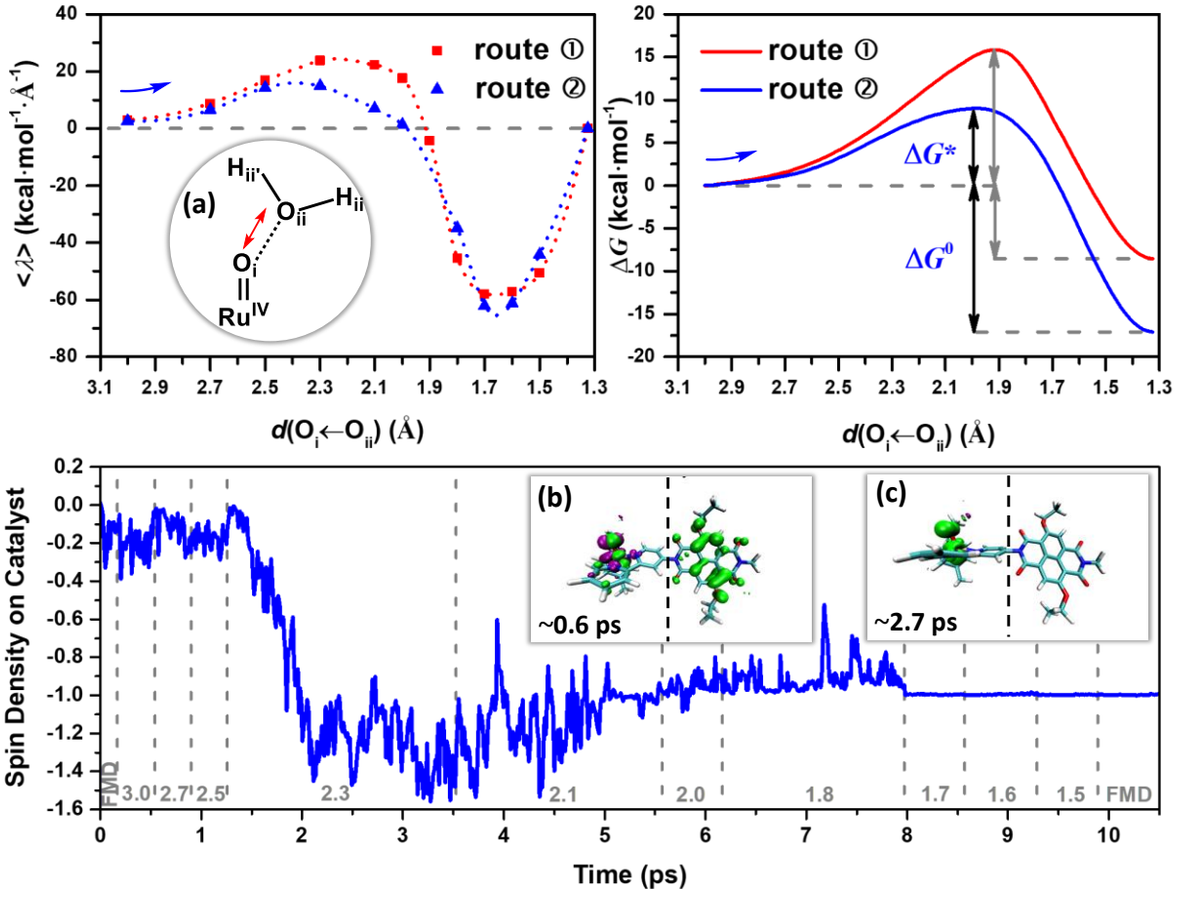

Figure 2.11. (top-left panel) Average constraint force represented by the Lagrangian multiplier $\langle\lambda\rangle$ computed for each constrained MD simulation of route ② (blue triangles) and ① (red squares, for comparison) as a function of the reaction coordinate $d(O_i \leftarrow O_{ii})$. The Akima spline (100 points) is used to interpolate the mean forces. The point at $d(O_i–O_{ii})$ = 1.32 Å corresponds to the equilibrium product state and thus its $\langle\lambda\rangle$ is assumed to be zero. (top-right panel) Free energy profile along the reaction coordinate $d(O_i \leftarrow O_{ii})$ of route ② computed from thermodynamic integration, compared to the results for route ①. (bottom panel) The spin density integrated over the half of the simulation box that includes the catalyst along the constrained and FMD trajectory of route ②. The value of the constrained reaction coordinate $d(O_i \leftarrow O_{ii})$ in the MD simulations is noted in grey. Inset (a) shows the schematic structure of the first water molecule along the hydrogen-bonding network coordinated to the oxygen ligand. The red double-sided arrow indicates the reaction coordinate considered for $[Ru^{IV}=O]^{2+}\cdots(H_2O)$ during the constrained MD simulations. Inset (b) and (c) show snapshots from the constrained MD trajectory, in which the spin density isosurface of α and β electrons in green and purple respectively. The labels refer to the time at which the snapshot has been taken along the collected trajectory.

(see Scheme 2.1 and Figure A2.8). However, the starting intermediate $^1([Ru^{IV}=O]^{2+}–NDI)$ before photooxidation turned out to be much higher in energy than $^3([Ru^{IV}=O]^{2+}–NDI)$ (see Figure A2.6, Tables A2.3 and A2.4).

2.3.3 Fourth Catalytic Water Oxidation Step

In this section we show that the NDI dye is definitely able to drive the subsequent fourth catalytic step. This is already evident by analyzing the free MD equilibration run carried out for 0.36 ps at the end of the third catalytic step, after having removed the excess proton from the simulation box. This MD trajectory shows that the $H_{ii'}$ proton of the hydroperoxo ligand is very weakly bound and essentially shared with the oxygen $O_{iii'}$ of an hydrogen-bonded water (see Scheme 2.2c), which is reflected in the temporary formation of the first H_3O^+ at the very beginning of the FMD simulation (see Figure 2.12, middle). In Figure 2.12 (top) the integrated spin density localized on the catalyst is also reported. Before photooxidation (dashed line in Figure 2.12) a value of –1 is found consistent with the doublet state of the catalyst. Thereafter, the oxidized intermediate $^3([Ru^{III}–OOH]^{2+}–NDI^{+\bullet})$ is formed by removing an electron from the simulation box. A sharp increase of the spin density localized on the catalyst is then observed after photooxidation, indicating an almost instantaneous electron transfer process from the catalyst to the oxidized $NDI^{+\bullet}$ dye and the generation of a second unpaired electron leading to a triplet state on the catalyst. In Figure 2.12 we show how the spin density rapidly moves from the oxidized $NDI^{+\bullet}$ dye to the Ru-based catalyst along the trajectory. At the same time, the $H_{ii'}$ proton is rapidly released by the O_{ii} atom and transferred to the neighboring water molecules (Figure 2.12, middle). This very fast PCET process (only ~50 fs after photooxidation of the NDI dye) leads to the final catalytic intermediate $^3([Ru^{II}–OO]^{2+}–NDI)$ (see eq. 2.4). This free AIMD simulation demonstrates that the fourth PCET catalytic water oxidation step occurs without any significant activation energy barrier. Similar electron and nuclear dynamics are observed along route ② for this catalytic step, which ends up with a less stable intermediate $^1([Ru^{II}–OO]^{2+}–NDI)$ (see more details in Figures A2.9 and A2.10, Tables A2.4 and A2.5). This is consistent with the O_2 ligand being more stable in the $S = 1$ state.

$$^3([Ru^{III}–OOH]^{2+}–NDI^{+\bullet}) \quad \leftrightarrow \quad ^3([Ru^{II}–OO]^{2+}–NDI) + H^+_{sol} \qquad (2.4)$$

After the proton transfer the distance between O_i and O_{ii} atoms shortens to an average value of ~1.24 Å (black line in Figure 2.12, bottom), confirming the formation of the O=O bond (for comparison, the O=O bond length in molecular O_2 is 1.21 Å). The final spin density mainly localizes on the two oxygen atoms (O_i

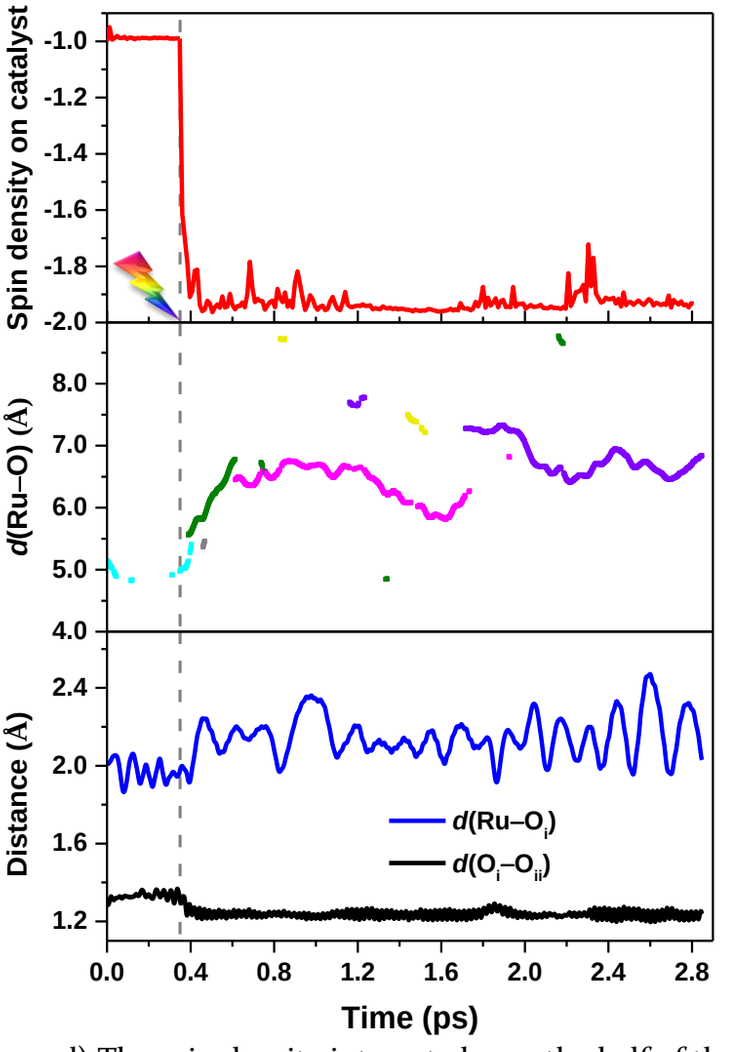

Figure 2.12. (top panel) The spin density integrated over the half of the simulation box including the catalyst before and after the photoinduced electron injection, which is mimicked by removing one electron from the system at 0.36 ps to generate an oxidized $^3([Ru^{III}–OOH]^{2+}–NDI^{+\bullet})$ (indicated by the grey dotted line). (middle panel) The distance between Ru and H_3O^+ measured for the free MD simulations. According to the simulations, the proton primarily bonds to four oxygens (cyan, dark green, magenta and purple). (bottom panel) Time evolution of the geometrical parameter d(Ru–O_i) (blue line) and d(O_i–O_{ii}) (black line) along the free MD trajectory (see labelling in Scheme 2.2c).

and O_{ii}), providing strong evidence for the generation of the triplet molecular O_2 product (see Figure 2.13). As a result, the Ru–O_i bond is considerably weakened (blue line in Figure 2.12, bottom), which indicates that the generated molecular O_2 can be easily exchanged with a water molecule in solution and thus regenerating the initial WOC state.

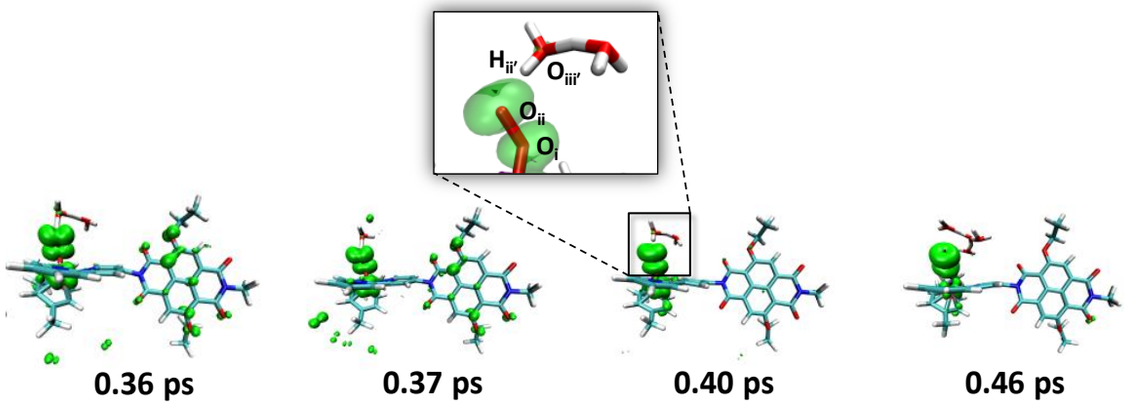

Figure 2.13. Spin density localization at different snapshots along the free MD trajectory for the final step in the catalytic cycle (see **Figure 2.12**). The hole (spin density) localized on the NDI immediately after photooxidation (0.36 ps) is very quickly filled by the electron from the catalyst within approximately 50 fs. In the snapshot taken at 0.4 ps the proton has been already transferred to the solvent water molecules nearby, temporarily forming a $(O_2H_5)^+$ complex (see enlarged inset above). The spin density at the end of the process is mostly localized on the O_2 ligand and shows the characteristic shape expected for the oxygen molecule (see also enlargement in the inset). A small amount of spin density can be seen localized on a few water molecules due to transient solvent polarization effects.

By analyzing the nuclear trajectory during the electron transfer process, we can observe a clear change in the dihedral angle (∠C1–N1–C2–C3, see Scheme 2.1) around the C–N bond connecting the NDI and the Ru catalyst from an average value of ~60° to 90 – 100°. In Figure A2.11 the evolution of this angle together with the spin density evolution is reported, suggesting a correlation between this torsional motion and the electron dynamics. Coherence in the electron and nuclear motion has been suggested to play a role in electron transfer processes both in natural and artificial systems.[54, 100] It might be interesting to further analyze the coupling between electronic and nuclear motion with quantum-classical simulations.

2.4. Conclusions

The whole photocatalytic water splitting cycle performed by the WOC–dye supramolecular complex $[Ru^{II}(H_2O)]^{2+}$–NDI dissolved in water has been systematically explored by means of DFT-based AIMD simulations at room temperature. The coupled electron and proton dynamics together with the solvent rearrangement are followed during the cycle, elucidating the catalytic mechanism of the four consecutive water oxidation steps.

The first three catalytic water oxidation steps are all exothermic with negative driving force ΔG^{o} after photooxidation of the NDI dye. The electron transfer from the catalyst to the oxidized dye always precedes the proton diffusion into the solvent bulk. The first and the second PCET catalytic steps present a similar small activation free energy barrier of the order of a few $k_B T$ at room temperature. The second PCET step has a larger driving force compared to the first, suggesting a much more stable product intermediate $^{3}([Ru^{IV}=O]^{2+}–NDI)$. The third PCET catalytic step involving the O–O bond formation with a second attacking water has a considerably higher activation energy barrier. This is the rate-limiting step where recombination processes from the semiconductor into the oxidized dye might indeed reduce the quantum efficiency of the whole process. One possible strategy to mitigate this issue is to add a molecular rectifier bridge between the dye and the semiconductor surface.[54] It is found that the antiparallel spin alignment of unpaired electrons on the WOC and dye is essential for the occurrence of the O–O bond formation. The rearrangement of solvent water molecules and formation of a hydrogen-bonding network during the MD simulations further facilitate the subsequent proton diffusion process. Interestingly, the fourth PCET step occurs immediately after the photooxidation of the NDI dye without any energy barrier, leading to the final intermediate with the O_2 ligand. All these results demonstrate that the selected NDI dye is a promising dye sensitizer to integrate in a DS-PEC device: it is able to perform fast electron injection into TiO_2 upon visible light absorption, and in its oxidized form can drive the whole photocatalytic water splitting cycle when properly coupled to the Ru-based catalyst. Considering that the NDI is capable of extracting electrons from the catalyst over the whole cycle, PCET conversion mediated by quantum overlap and vibrationally assisted is a mechanism that may be difficult to suppress, which works to the advantage of smooth catalysis.[101-102]

Further progress aimed at lowering the activation energy barrier of the third PCET catalytic step can be achieved by introducing extra proton acceptors[103-108] near the active site, and/or by assembling the catalyst near an IEM[109-113] between the anode and cathode chambers, which would create a favorable environment to facilitate the proton release and transport through the membrane.

2.5 References

[1] Dresselhaus, M. S.; Thomas, I. L. *Nature* **2001**, *414*, 332-337.
[2] Chynoweth, D. P.; Owens, J. M.; Legrand, R. *Renewable Energy* **2001**, *22*, 1-8.
[3] Lewis, N. S. *Science* **2007**, *315*, 798-801.
[4] Nocera, D. G. *Acc. Chem. Res.* **2012**, *45*, 767-776.
[5] Gust, D.; Moore, T. A.; Moore, A. L. *Acc. Chem. Res.* **2009**, *42*, 1890-1898.
[6] Zaharieva, I.; Wichmann, J. M.; Dau, H. *J. Biol. Chem.* **2011**, *286*, 18222-18228.
[7] Tachibana, Y.; Vayssieres, L.; Durrant, J. R. *Nat. Photonics* **2012**, *6*, 511-518.
[8] Dau, H.; Zaharieva, I.; Haumann, M. *Curr. Opin. Chem. Biol.* **2012**, *16*, 3-10.
[9] Jafari, T.; Moharreri, E.; Amin, A.; Miao, R.; Song, W.; Suib, S. *Molecules* **2016**, *21*, 900.
[10] Kim, W.; Edri, E.; Frei, H. *Acc. Chem. Res.* **2016**, *49*, 1634-1645.
[11] Xiang, C.; Weber, A. Z.; Ardo, S.; Berger, A.; Chen, Y.; Coridan, R.; Fountaine, K. T.; Haussener, S.; Hu, S.; Liu, R.; et al. *Angew. Chem., Int. Ed.* **2016**, *55*, 12974-12988.
[12] Turan, B.; Becker, J.-P.; Urbain, F.; Finger, F.; Rau, U.; Haas, S. *Nat. Commun.* **2016**, *7*, 12681.
[13] Grätzel, M. *Nature* **2001**, *414*, 338-344.
[14] Liu, C.; Colón, B. C.; Ziesack, M.; Silver, P. A.; Nocera, D. G. *Science* **2016**, *352*, 1210-1213.
[15] Haas, T.; Krause, R.; Weber, R.; Demler, M.; Schmid, G. *Nat. Catal.* **2018**, *1*, 32-39.
[16] Inoue, H.; Shimada, T.; Kou, Y.; Nabetani, Y.; Masui, D.; Takagi, S.; Tachibana, H. *ChemSusChem* **2011**, *4*, 173-179.
[17] Yu, Z.; Li, F.; Sun, L. *Energy Environ. Sci.* **2015**, *8*, 760-775.
[18] Peerakiatkhajohn, P.; Yun, J.-H.; Wang, S.; Wang, L. *J. Photonics Energy* **2016**, *7*, 012006.
[19] Ding, X.; Gao, Y.; Ye, L.; Zhang, L.; Sun, L. *ChemSusChem* **2015**, *8*, 3992-3995.
[20] Moniz, S. J. A.; Shevlin, S. A.; Martin, D. J.; Guo, Z.-X.; Tang, J. *Energy Environ. Sci.* **2015**, *8*, 731-759.
[21] Hetterscheid, D. G. H.; Reek, J. N. H. *Angew. Chem., Int. Ed.* **2012**, *51*, 9740-9747.
[22] Concepcion, J. J.; Jurss, J. W.; Brennaman, M. K.; Hoertz, P. G.; Patrocinio, A. O. T.; Murakami Iha, N. Y.; Templeton, J. L.; Meyer, T. J. *Acc. Chem. Res.* **2009**, *42*, 1954-1965.
[23] Duan, L.; Xu, Y.; Gorlov, M.; Tong, L.; Andersson, S.; Sun, L. *Chem. - Eur. J.* **2010**, *16*, 4659-4668.
[24] Prévot, M. S.; Sivula, K. *J. Phys. Chem. C* **2013**, *117*, 17879-17893.
[25] Swierk, J. R.; Mallouk, T. E. *Chem. Soc. Rev.* **2013**, *42*, 2357-2387.
[26] Luo, J.; Im, J.-H.; Mayer, M. T.; Schreier, M.; Nazeeruddin, M. K.; Park, N.-G.; Tilley, S. D.; Fan, H. J.; Grätzel, M. *Science* **2014**, *345*, 1593-1596.
[27] Liu, J.; Liu, Y.; Liu, N.; Han, Y.; Zhang, X.; Huang, H.; Lifshitz, Y.; Lee, S.-T.; Zhong, J.; Kang, Z. *Science* **2015**, *347*, 970-974.
[28] Swierk, J. R.; Méndez-Hernández, D. D.; McCool, N. S.; Liddell, P.; Terazono, Y.; Pahk, I.; Tomlin, J. J.; Oster, N. V.; Moore, T. A.; Moore, A. L.; et al. *Proc. Natl. Acad. Sci. U. S. A.* **2015**, *112*, 1681-1686.
[29] Verlage, E.; Hu, S.; Liu, R.; Jones, R. J. R.; Sun, K.; Xiang, C.; Lewis, N. S.; Atwater, H. A. *Energy Environ. Sci.* **2015**, *8*, 3166-3172.
[30] de Respinis, M.; Joya, K. S.; De Groot, H. J. M.; D'Souza, F.; Smith, W. A.; van de Krol, R.; Dam, B. *J. Phys. Chem. C* **2015**, *119*, 7275-7281.
[31] Ding, X.; Zhang, L.; Wang, Y.; Liu, A.; Gao, Y. *Coord. Chem. Rev.* **2018**, *357*, 130-143.
[32] Brennaman, M. K.; Dillon, R. J.; Alibabaei, L.; Gish, M. K.; Dares, C. J.; Ashford, D. L.; House, R. L.; Meyer, G. J.; Papanikolas, J. M.; Meyer, T. J. *J. Am. Chem. Soc.* **2016**, *138*, 13085-13102.
[33] Dau, H.; Limberg, C.; Reier, T.; Risch, M.; Roggan, S.; Strasser, P. *ChemCatChem* **2010**, *2*, 724-761.
[34] Hughes, T. F.; Friesner, R. A. *J. Phys. Chem. B* **2011**, *115*, 9280-9289.

[35] Akimov, A. V.; Neukirch, A. J.; Prezhdo, O. V. *Chem. Rev.* **2013**, *113*, 4496-4565.

[36] McCool, N. S.; Swierk, J. R.; Nemes, C. T.; Saunders, T. P.; Schmuttenmaer, C. A.; Mallouk, T. E. *ACS Appl. Mater. Interfaces* **2016**, *8*, 16727-16735.

[37] Concepcion, J. J.; Tsai, M.-K.; Muckerman, J. T.; Meyer, T. J. *J. Am. Chem. Soc.* **2010**, *132*, 1545-1557.

[38] Pastore, M. *Computation* **2017**, *5*, 5.

[39] de Ruiter, J. M.; Purchase, R. L.; Monti, A.; van der Ham, C. J. M.; Gullo, M. P.; Joya, K. S.; D'Angelantonio, M.; Barbieri, A.; Hetterscheid, D. G. H.; de Groot, H. J. M.; et al. *ACS Catal.* **2016**, *6*, 7340-7349.

[40] Monti, A.; de Ruiter, J. M.; de Groot, H. J. M.; Buda, F. *J. Phys. Chem. C* **2016**, *120*, 23074-23082.

[41] Meyer, T. J.; Huynh, M. H. V.; Thorp, H. H. *Angew. Chem., Int. Ed.* **2007**, *46*, 5284-5304.

[42] Hammes-Schiffer, S. *Energy Environ. Sci.* **2012**, *5*, 7696-7703.

[43] Hammes-Schiffer, S. *J. Am. Chem. Soc.* **2015**, *137*, 8860-8871.

[44] Huynh, M. H. V.; Meyer, T. J. *Chem. Rev.* **2007**, *107*, 5004-5064.

[45] Kishore, R. S. K.; Kel, O.; Banerji, N.; Emery, D.; Bollot, G.; Mareda, J.; Gomez-Casado, A.; Jonkheijm, P.; Huskens, J.; Maroni, P.; et al. *J. Am. Chem. Soc.* **2009**, *131*, 11106-11116.

[46] Sakai, N.; Mareda, J.; Vauthey, E.; Matile, S. *Chem. Commun.* **2010**, *46*, 4225-4237.

[47] Diac, A.; Matache, M.; Grosu, I.; Hădade, N. D. *Adv. Synth. Catal.* **2018**, *360*, 817-845.

[48] Earmme, T.; Hwang, Y.-J.; Murari, N. M.; Subramaniyan, S.; Jenekhe, S. A. *J. Am. Chem. Soc.* **2013**, *135*, 14960-14963.

[49] Choi, J.; Kim, K.-H.; Yu, H.; Lee, C.; Kang, H.; Song, I.; Kim, Y.; Oh, J. H.; Kim, B. J. *Chem. Mater.* **2015**, *27*, 5230-5237.

[50] Kim, T.; Kim, J.-H.; Kang, T. E.; Lee, C.; Kang, H.; Shin, M.; Wang, C.; Ma, B.; Jeong, U.; Kim, T.-S.; et al. *Nat. Commun.* **2015**, *6*, 8547.

[51] Ambrosio, F.; Martsinovich, N.; Troisi, A. *J. Phys. Chem. Lett.* **2012**, *3*, 1531-1535.

[52] Zhang, L.; Cole, J. M. *ACS Appl. Mater. Interfaces* **2015**, *7*, 3427-3455.

[53] Materna, K. L.; Crabtree, R. H.; Brudvig, G. W. *Chem. Soc. Rev.* **2017**, *46*, 6099-6110.

[54] Monti, A.; Negre, C. F. A.; Batista, V. S.; Rego, L. G. C.; de Groot, H. J. M.; Buda, F. *J. Phys. Chem. Lett.* **2015**, *6*, 2393-2398.

[55] Monti, A.; de Groot, H. J. M.; Buda, F. *J. Phys. Chem. C* **2014**, *118*, 15600-15609.

[56] Bernasconi, L.; Kazaryan, A.; Belanzoni, P.; Baerends, E. J. *ACS Catal.* **2017**, *7*, 4018-4025.

[57] Swart, M.; Ehlers, A. W.; Lammertsma, K. *Mol. Phys.* **2004**, *102*, 2467-2474.

[58] Carvalho, A. T. P.; Swart, M. *J. Chem. Inf. Model* **2014**, *54*, 613-620.

[59] Groenhof, A. R.; Ehlers, A. W.; Lammertsma, K. *J. Am. Chem. Soc.* **2007**, *129*, 6204-6209.

[60] Conradie, J.; Ghosh, A. *J. Chem. Theory Comput.* **2007**, *3*, 689-702.

[61] Vallés-Pardo, J. L.; Guijt, M. C.; Iannuzzi, M.; Joya, K. S.; de Groot, H. J. M.; Buda, F. *ChemPhysChem* **2012**, *13*, 140-146.

[62] Liao, M.-S.; Watts, J. D.; Huang, M.-J. *J. Phys. Chem. A* **2007**, *111*, 5927-5935.

[63] Güell, M.; Luis, J. M.; Siegbahn, P. E. M.; Solà, M. *J. Biol. Inorg. Chem.* **2009**, *14*, 273-285.

[64] Klamt, A. *J. Phys. Chem.* **1995**, *99*, 2224-2235.

[65] Klamt, A.; Jonas, V. *J. Chem. Phys.* **1996**, *105*, 9972-9981.

[66] Te Velde, G.; Bickelhaupt, F. M.; Baerends, E. J.; Fonseca Guerra, C.; van Gisbergen, S. J. A.; Snijders, J. G.; Ziegler, T. *J. Comput. Chem.* **2001**, *22*, 931-967.

[67] ADF2017, SCM, Theoretical Chemistry, Vrije Universiteit, Amsterdam, The Netherlands, http://www.scm.com.

[68] Ma, C.; Piccinin, S.; Fabris, S. *ACS Catal.* **2012**, *2*, 1500-1506.

[69] CPMD, http://www.cpmd.org, Copyright IBM Corp., 1990–2019, Copyright MPI für Festkörperforschung Stuttgart, 1997–2001.

[70] Accelrys Software Inc., *Discovery Studio Modeling Environment*, Accelrys Software Inc., San Diego, **2012**.

[71] Brooks, B. R.; Bruccoleri, R. E.; Olafson, B. D.; States, D. J.; Swaminathan, S.; Karplus, M. *J. Comput. Chem.* **1983**, *4*, 187-217.
[72] Hartwigsen, C.; Goedecker, S.; Hutter, J. *Phys. Rev. B* **1998**, *58*, 3641-3662.
[73] Lin, I. C.; Coutinho-Neto, M. D.; Felsenheimer, C.; von Lilienfeld, O. A.; Tavernelli, I.; Rothlisberger, U. *Phys. Rev. B* **2007**, *75*, 205131.
[74] Humphrey, W.; Dalke, A.; Schulten, K. VMD: visual molecular dynamics. *J. Mol. Graphics* **1996**, *14*, 33-38.
[75] VMD - Visual Molecular Dynamics, Theoretical Chemistry and Computational Biophysics Group, University Of Illinois, Urbana, U.S.A, **2016**.
[76] Ciccotti, G.; Ferrario M. *Mol. Simul.* **2004**, *30*, 787-793.
[77] Ensing, B.; Meijer, E. J.; Blöchl, P. E.; Baerends, E. J. *J. Phys. Chem. A* **2001**, *105*, 3300-3310.
[78] Costanzo, F.; Della Valle, R. G. *J. Phys. Chem. B* **2008**, *112*, 12783-12789.
[79] Otter, W. K. d.; Briels, W. J. *J. Chem. Phys.* **1998**, *109*, 4139-4146.
[80] Sprik, M.; Ciccotti, G. *J. Chem. Phys.* **1998**, *109*, 7737-7744.
[81] Bernasconi, L.; Baerends, E. J.; Sprik, M. *J. Phys. Chem. B* **2006**, *110*, 11444-11453.
[82] de Grotthuss, C. J. T. *Biochim. Biophys. Acta, Bioenerg.* **2006**, *1757*, 871-875.
[83] Agmon, N. *Chem. Phys. Lett.* **1995**, *244*, 456-462.
[84] Cukierman, S. Et tu, *Biochim. Biophys. Acta, Bioenerg.* **2006**, *1757*, 876-885.
[85] Markovitch, O.; Chen, H.; Izvekov, S.; Paesani, F.; Voth, G. A.; Agmon, N. *J. Phys. Chem. B* **2008**, *112*, 9456-9466.
[86] Hassanali, A.; Giberti, F.; Cuny, J.; Kühne, T. D.; Parrinello, M. *Proc. Natl. Acad. Sci.* **2013**, *110*, 13723-13728.
[87] Marx, D.; Chandra, A.; Tuckerman, M. E. *Chem. Rev.* **2010**, *110*, 2174-2216.
[88] Codorniu-Hernández, E.; Kusalik, P. G. *Proc. Natl. Acad. Sci.* **2013**, *110*, 13697-13698.
[89] Liang, R.; Li, H.; Swanson, J. M. J.; Voth, G. A. *Proc. Natl. Acad. Sci.* **2014**, *111*, 9396-9401.
[90] Yang, X.; Hall, M. B. *J. Am. Chem. Soc.* **2010**, *132*, 120-130.
[91] Lundberg, M.; Siegbahn, P. E. M. *Chem. Phys. Lett.* **2005**, *401*, 347-351.
[92] Siegbahn, P. E. M. *Chem. - Eur. J.* **2006**, *12*, 9217-9227.
[93] Guo, Y.; Li, H.; He, L.-L.; Zhao, D.-X.; Gong, L.-D.; Yang, Z.-Z. *Phys. Chem. Chem. Phys.* **2017**, *19*, 13909-13923.
[94] Eyring, H. *J. Chem. Phys.* **1935**, *3*, 107-115.
[95] Laidler, K. J.; King, M. C. *J. Phys. Chem.* **1983**, *87*, 2657-2664.
[96] Pollak, E.; Talkner, P. *Chaos* **2005**, *15*, 026116.
[97] Solis, B. H.; Hammes-Schiffer, S. *Inorg. Chem.* **2014**, *53*, 6427-6443.
[98] Gish, M. K.; Lapides, A. M.; Brennaman, M. K.; Templeton, J. L.; Meyer, T. J.; Papanikolas, J. M. *J. Phys. Chem. Lett.* **2016**, *7*, 5297-5301.
[99] Chou, H.-H.; Yang, C.-H.; Lin, J. T. s.; Hsu, C.-P. *J. Phys. Chem. C* **2017**, *121*, 983-992.
[100] Scholes, G. D. *J. Phys. Chem. Lett.* **2018**, *9*, 1568-1572.
[101] Bruno, W. J.; Bialek, W., *Biophys. J.* **1992**, *63*, 689-699.
[102] Moser, C. C.; Keske, J. M.; Warncke, K.; Farid, R. S.; Dutton, P. L., *Nature* **1992**, *355*, 796-802.
[103] Chen, Z.; Concepcion, J. J.; Hu, X.; Yang, W.; Hoertz, P. G.; Meyer, T. J. *Proc. Natl. Acad. Sci.* **2010**, *107*, 7225-7229.
[104] Hammes-Schiffer, S. *Acc. Chem. Res.* **2009**, *42*, 1881-1889.
[105] Shaffer, D. W.; Xie, Y.; Concepcion, J. J. *Chem. Soc. Rev.* **2017**, *46*, 6170-6193.
[106] Shaffer, D. W.; Xie, Y.; Szalda, D. J.; Concepcion, J. J. *J. Am. Chem. Soc.* **2017**, *139*, 15347-15355.
[107] Meyer, T. J.; Sheridan, M. V.; Sherman, B. D. *Chem. Soc. Rev.* **2017**, *46*, 6148-6169.
[108] Coggins, M. K.; Zhang, M. T.; Chen, Z.; Song, N.; Meyer, T. J. *Angew. Chem., Int. Ed.* **2014**, *53*, 12226-12230.

[109] Varcoe, J. R.; Atanassov, P.; Dekel, D. R.; Herring, A. M.; Hickner, M. A.; Kohl, P. A.; Kucernak, A. R.; Mustain, W. E.; Nijmeijer, K.; Scott, K.; et al. *Energy Environ. Sci.* **2014**, *7*, 3135-3191.
[110] Ran, J.; Wu, L.; He, Y.; Yang, Z.; Wang, Y.; Jiang, C.; Ge, L.; Bakangura, E.; Xu, T. *J. Membr. Sci.* **2017**, *522*, 267-291.
[111] Gu, S.; Gong, K.; Yan, E. Z.; Yan, Y. *Energy Environ. Sci.* **2014**, *7*, 2986-2998.
[112] He, G.; Li, Z.; Zhao, J.; Wang, S.; Wu, H.; Guiver, M. D.; Jiang, Z. *Adv. Mater.* **2015**, *27*, 5280-5295.
[113] Hammarström, L. *Acc. Chem. Res.* **2015**, *48*, 840-850.

A. Appendix

2.A.1. Calculated and Experimentally Measured Free Energy Change for each Catalytic Step along the Proposed Catalytic Mechanism

Table A2.1. Calculated ΔG_{calc} for each catalytic step along the proposed catalytic mechanism computed with the ADF program[1-2] at the OPBE/TZP level, in comparison to the experimentally measured ΔG_{exp} for $[Ru^{II}–OH_2]^{2+}$ water oxidation catalyst (WOC) adjusted to pH 0 according to the Nernst Equation (adapted from Ref. 44 in the main text).

Step	Intermediates		ΔG_{calc} (eV)	ΔG_{exp} (eV)
1st	$[Ru^{II}–OH_2]^{2+} \rightarrow [Ru^{III}–OH]^{2+}$	$(I_1 \rightarrow I_2)$	0.87	0.67
2nd	$[Ru^{III}–OH]^{2+} \rightarrow [Ru^{IV}=O]^{2+}$	$(I_2 \rightarrow I_3)$	1.38	1.27
3rd	$[Ru^{IV}=O]^{2+} \rightarrow [Ru^{III}–OOH]^{2+}$	$(I_3 \rightarrow I_4)$	2.19	1.83
4th	$[Ru^{III}–OOH]^{2+} \rightarrow [Ru^{II}–OO]^{2+}$	$(I_4 \rightarrow I_0)$	0.73	
	$[Ru^{II}–OO]^{2+} \rightarrow [Ru^{II}–OH_2]^{2+}$	$(I_0 \rightarrow I_1)$	-0.15	
	$2H_2O \rightarrow 2H_2 + O_2$		5.02	4.92

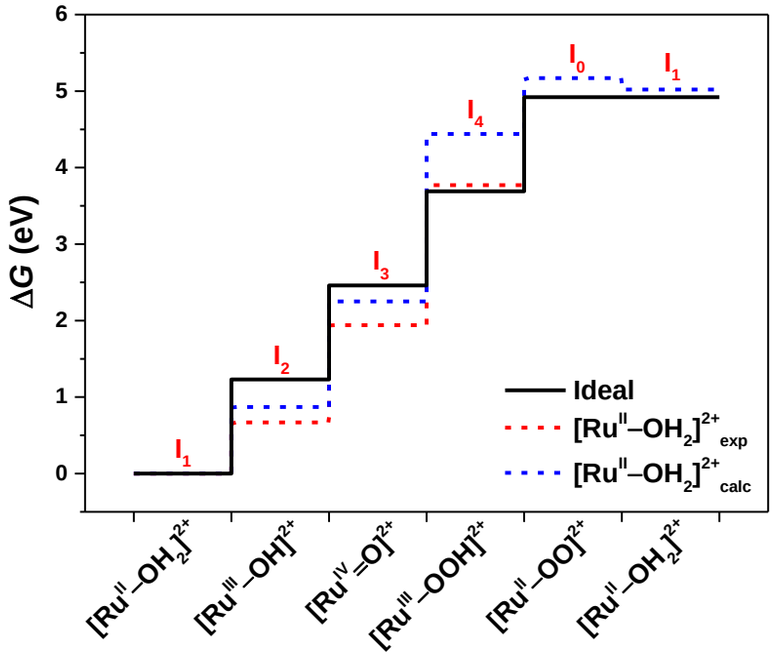

Figure A2.1. Free energy difference ΔG between intermediates along the catalytic pathway of the $[Ru^{II}–OH_2]^{2+}$ catalyst. DFT results (dashed blue line) are compared with the values extracted from electrochemical data (dashed red line). We also show for comparison the optimal catalyst case (black line) corresponding to a change in free energy of 1.23 eV for all four steps (adapted from Ref. 44 in the main text).

2.A.2. Frontier Molecular Orbital Energy Levels of four Intermediates along the Catalytic Pathway of the $[Ru^{II}–OH_2]^{2+}$ Catalyst

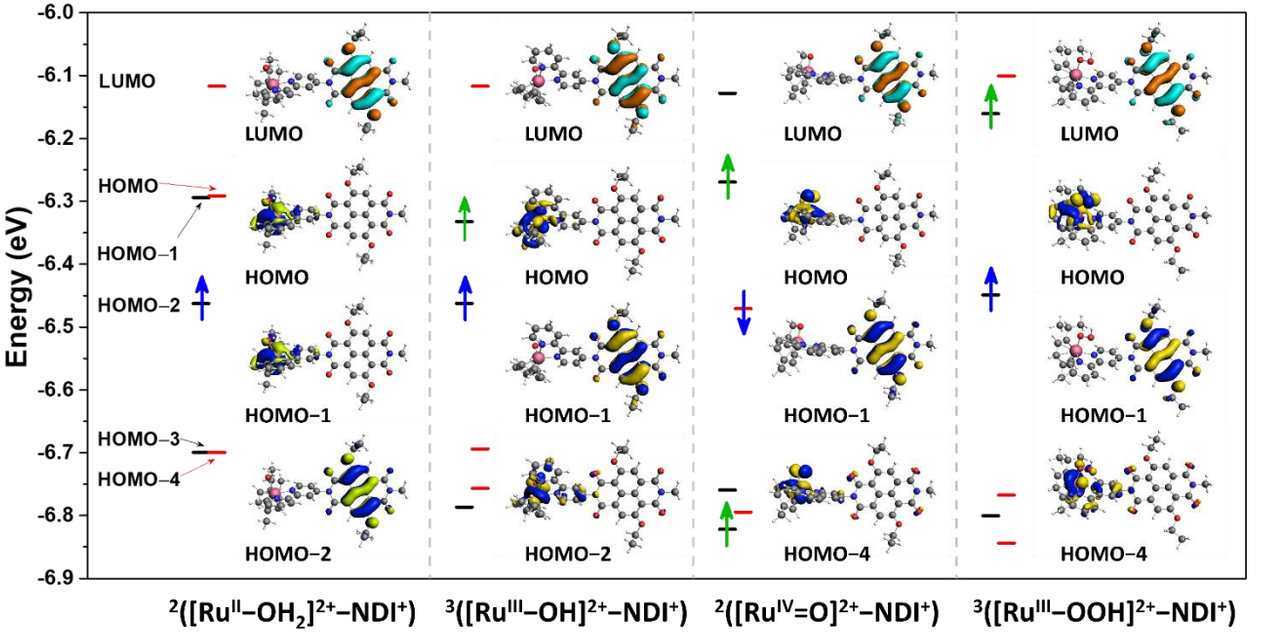

Figure A2.2. Selected frontier molecular orbitals of involved intermediates after photooxidation of NDI during the four consecutive catalytic steps in route ① computed with the ADF program using the OPBE functional and the TZP basis set. The continuum solvation model COSMO[3-4] is used to describe the water environment. The left (black) and right (red) columns refer to as the α orbitals and β orbitals, respectively. Only the unpaired electrons are indicated by vertical arrows explicitly (green for unpaired electron localized on the catalyst and blue for unpaired electron on the oxidized $NDI^{+\bullet}$). See Table A2.2 for the molecular energy levels.

For all these intermediates, the partially occupied molecular orbital localized on the NDI is always lower in energy than the HOMO of the supramolecular complex, which is localized on the ruthenium catalyst. This result suggests that for all the oxidized intermediates there is a driving force for electron transfer from the ruthenium catalyst to the NDI dye in continuum solvation model. The AIMD simulations presented in this work show that this is also the case in explicit solvent.

Table A2.2. Selected frontier molecular orbital energy levels and energy difference ΔE_{SOMO} (in eV) between SOMO WOC (HOMO WOC for $^2([Ru^{II}–OH_2]^{2+}–NDI^{+\bullet})$) and SOMO dye of four intermediates along the catalytic pathway of the $[Ru^{II}–OH_2]^{2+}$ catalyst following route ① in Scheme 2.1 computed with the ADF program using the OPBE (and PBE for comparison) functional and the TZP basis set. The continuum solvation model COSMO is used to describe the water environment. Only the unpaired electrons are indicated by vertical arrows explicitly (green for unpaired electron localized on the catalyst and blue for unpaired electron on the oxidized $NDI^{+\bullet}$).

Intermediate		$^2([Ru^{II}–OH_2]^{2+}–NDI^{+\bullet})$			$^3([Ru^{III}–OH]^{2+}–NDI^{+\bullet})$			$^2([Ru^{IV}=O]^{2+}–NDI^{+\bullet})$			$^3([Ru^{III}–OOH]^{2+}–NDI^{+\bullet})$		
		↑			↑	↑		↑	↑	↓		↑	↑
							OPBE						
Energy levels		**Orbital**	**Energy**		**Orbital**	**Energy**		**Orbital**	**Energy**		**Orbital**	**Energy**	
LUMO	*β*		–6.1172	*β*		–6.1144	*α*		–6.1226	*β*		–6.1008	
HOMO	*β*	} (*HOMO WOC*)	–6.2913	*α*	(*SOMO WOC*)	–6.3430	*α*	(*SOMO WOC*)	–6.2750	*α*	(*SOMO WOC*)	–6.1607	
HOMO–1	*α*		–6.2940	*α*	(*SOMO dye*)	–6.4600	*β*	(*SOMO dye*)	–6.4682	*α*	(*SOMO dye*)	–6.4491	
HOMO–2	*α*	(*SOMO dye*)	–6.4628	*β*		–6.6804	*α*		–6.7321	*β*		–6.7675	
HOMO–3	*β*		–6.6995	*β*		–6.7566	*β*		–6.7648	*α*		–6.8002	
HOMO–4	*α*		–6.6995	*α*		–6.7920	*α*		–6.8274	*β*		–6.8437	
ΔE_{SOMO}			0.1714			0.1170			0.1932			0.2884	
							PBE						
Energy levels		**Orbital**	**Energy**		**Orbital**	**Energy**		**Orbital**	**Energy**		**Orbital**	**Energy**	
LUMO	*β*		–6.1172	*β*		–6.1226	*α*		–6.1281	*β*		–6.1281	
HOMO	*β*	} (*HOMO WOC*)	–6.2723	*α*	(*SOMO WOC*)	–6.3512	*α*	(*SOMO WOC*)	–6.2641	*α*	(*SOMO WOC*)	–6.1852	
HOMO–1	*α*		–6.2723	*α*	(*SOMO dye*)	–6.4355	*β*	(*SOMO dye*)	–6.4383	*α*	(*SOMO dye*)	–6.4410	
HOMO–2	*α*	(*SOMO dye*)	–6.4301	*β*		–6.6886	*α*		–6.7213	*β*		–6.7321	
HOMO–3	*β*		–6.5716	*β*		–6.7349	*α*		–6.7430	*α*		–6.7539	
HOMO–4	*α*		–6.5743	*α*		–6.7566	*β*		–6.7458	*β*		–6.8954	
ΔE_{SOMO}			0.1578			0.0844			0.1742			0.2558	

2.A.3. The Constraint Force and Running Average of the Constraint Force as a Function of Time

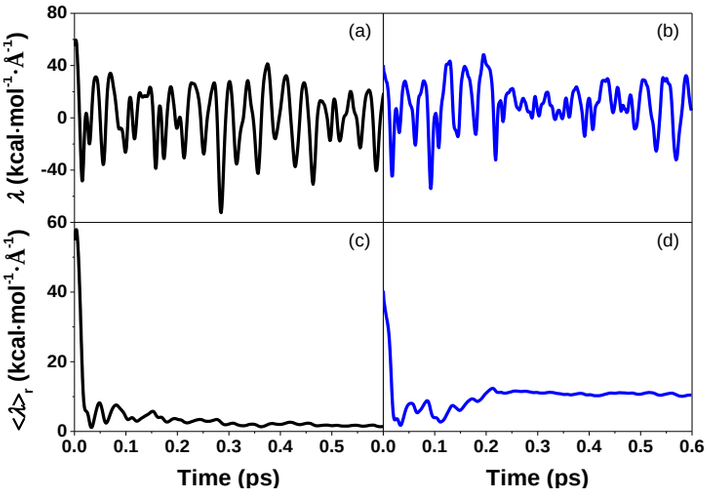

Figure A2.3. The constraint force (λ, in kcal mol^{-1} Å^{-1}) and running average of the constraint force ($\langle\lambda\rangle_r$, in kcal mol^{-1} Å^{-1}) as a function of time for two different distance constraints $d(H_i \leftarrow O_{ii})$ = 1.6 Å (a, c) and $d(H_i \leftarrow O_{ii})$ = 1.4 Å (b, d), respectively. The running average reaches a stable value even within this relatively short MD timescale of ~0.5 ps.

2.A.4. Standard Deviation of Free Energy Profiles along the Reaction Coordinate *d*(Hi←Oii)

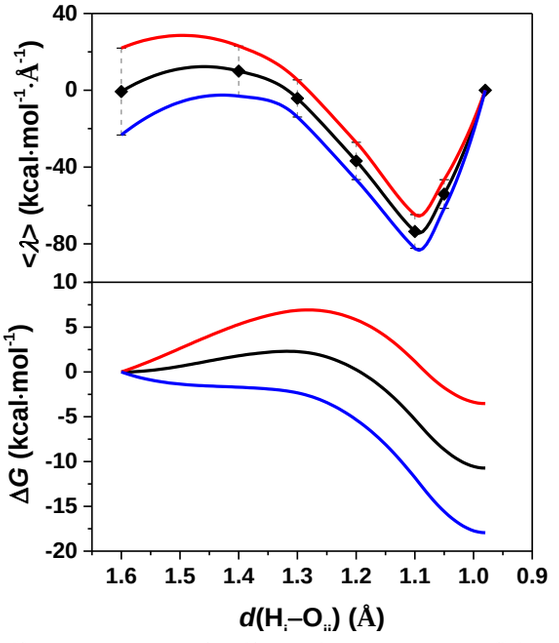

Figure A2.4. (top panel) Maximum (red) and minimum (blue) interpolations of the Lagrangian multiplier $\langle\lambda\rangle$ reproduced from Figure 2.4. The error bars indicate the standard deviations. (bottom panel) Free energy profiles along the reaction coordinate $d(H_i \leftarrow O_{ii})$ computed from thermodynamic integration of the interpolated time-averaged mean forces.

2.A.5. The Results with Antiparallel Spin Alignment on NDI along the MD Trajectories of second Catalytic Step in Route ②

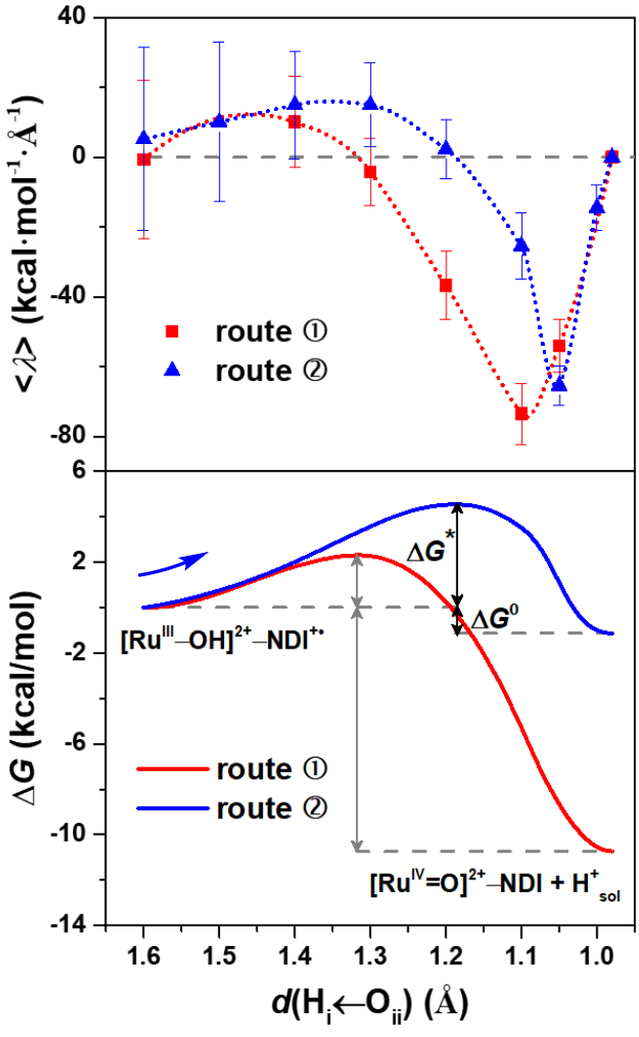

Figure A2.5. (top panel) The constraint mean force represented by the Lagrangian multiplier $\langle\lambda\rangle$ computed for each constrained MD simulation as a function of the reaction coordinate $d(H_i \leftarrow O_{ii})$ along route ② (blue triangles) and ① (red squares), for comparison. The mean force at the equilibrium distance $d(H_i–O_{ii})$ = 0.98 Å evaluated in the free MD has been set to 0. The 100-point Akima spline interpolation (dotted lines) is used to interpolate the mean forces including also the zero point at equilibrium. (bottom panel) Free energy profile along the reaction coordinate $d(H_i \leftarrow O_{ii})$ of route ② (blue line) and ① (red line) computed from thermodynamic integration of the interpolated time-averaged mean forces. The initial and final intermediates are also indicated.

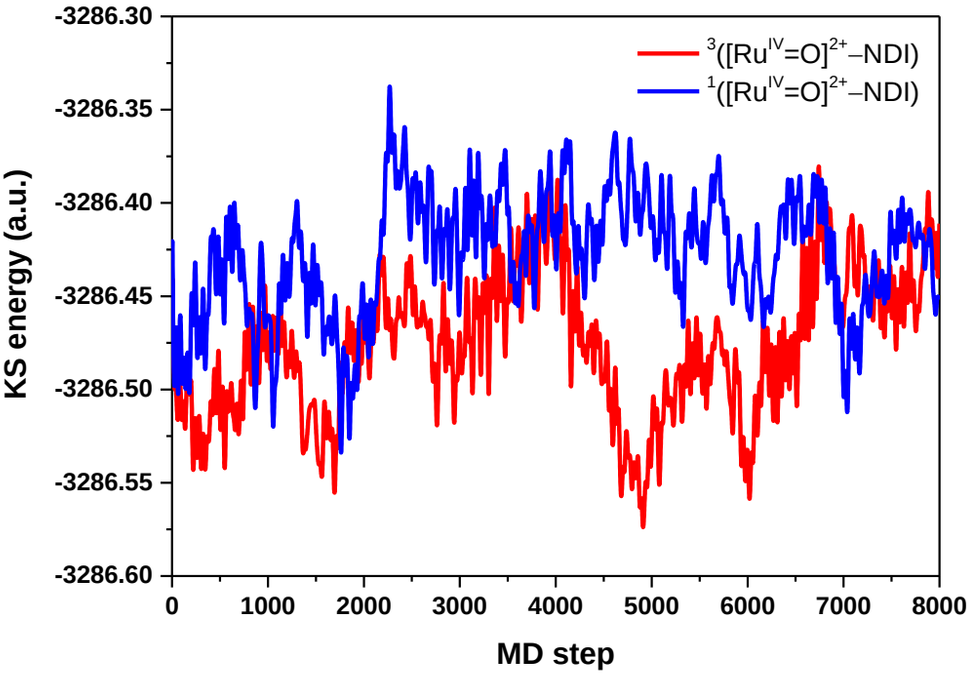

Figure A2.6. Time evolution of the KS energy of the product intermediates $^3([Ru^{IV}=O]^{2+}–NDI)$ (red line) and $^1([Ru^{IV}=O]^{2+}–NDI)$ (blue line) along the FMD trajectories after the second catalytic step. Although large energy fluctuations are observed during the MD simulations, the product intermediate $^3([Ru^{IV}=O]^{2+}–NDI)$ is on average lower in energy than $^1([Ru^{IV}=O]^{2+}–NDI)$ (see Table A2.3).

Table A2.3. Time-averaged KS energy of the product intermediates $^3([Ru^{IV}=O]^{2+}–NDI)$ and $^1([Ru^{IV}=O]^{2+}–NDI)$ and the energy difference (ΔE_{int}) between them along the free MD trajectories (see Figure A2.6).

2*S*+1	**$[Ru^{IV}=O]^{2+}$–NDI**	**KS energy** (eV)	**ΔE_{int}** (eV)
3	↑ ↑	–89429.615	1.313
1	↑ ↓	–89428.302	

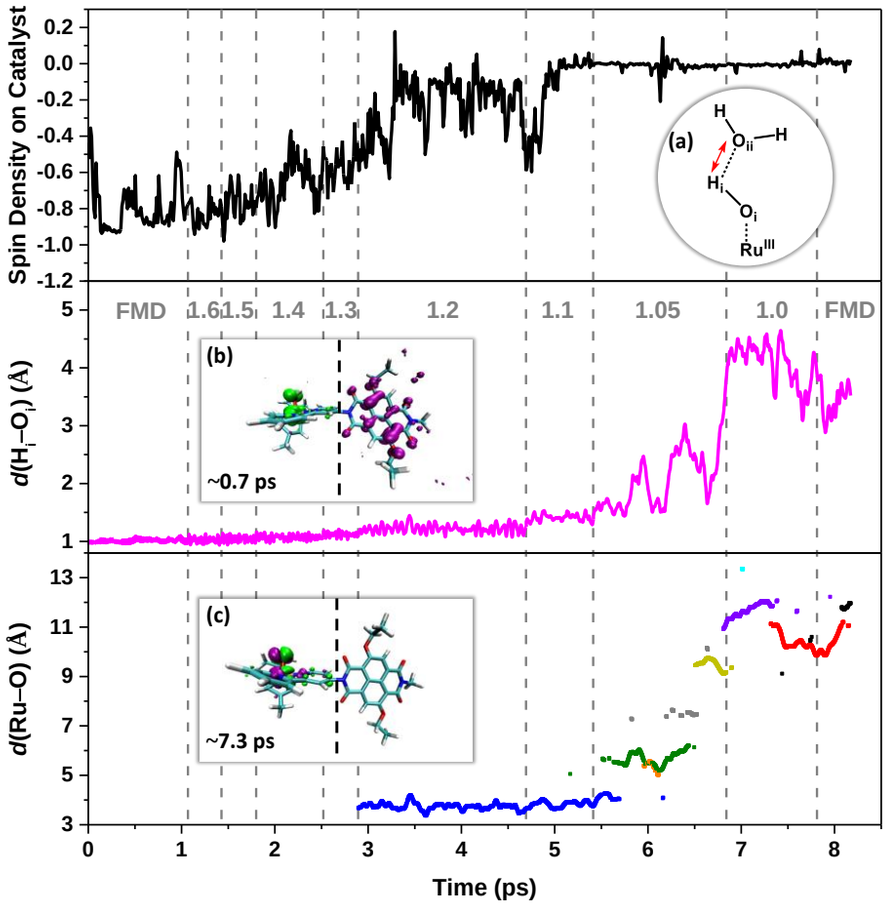

Figure A2.7. (top panel) The spin density integrated over the half of the simulation box including the catalyst (left-hand side of the dashed black line in the inset **b** and **c**) along the MD trajectories starting from the oxidized intermediate $^{1}([Ru^{III}–OH]^{2+}–NDI^{+\bullet})$ (see route ② in Scheme 1). An integrated spin density value of –1 corresponds to one unpaired α electron. The starting configuration at $d(H_i \leftarrow O_{ii})$ = 1.6 Å has been extracted from a previous unconstrained simulation of the first catalytic intermediate for ~1 ps (with an average $d(H_i–O_{ii}) \approx 1.7$ Å). (middle panel) Time evolution of the geometrical parameter $d(H_i–O_i)$ along the constrained and FMD trajectory. (bottom panel) The distance between Ru and H_3O^+, defined as an oxygen atom with 3 H within a radius of 1.2 Å, as measured for a sequence of MD simulations. According to the simulations, only one oxygen is in the H_3O^+ form at any time, and although the proton associates with a number of different oxygens (indicated with different colours) during the simulation, it is primarily bonded to four oxygens (blue, gold, red and purple). The value of the constrained reaction coordinate $d(H_i \leftarrow O_{ii})$ applied in the MD simulations is noted in grey. Inset (a) shows the schematic structure of the first few water molecules along the hydrogen-bonding network coordinated to the hydroxide ligand. The red double-sided arrow indicates the reaction coordinate considered for oxidized intermediate $^{1}([Ru^{III}–OH]^{2+}–NDI^{+\bullet})$ during the constrained MD simulations. Inset (b) and (c) show snapshots from the FMD and constrained MD trajectories, in which the spin density isosurface of α and β electrons in green and purple respectively. The labels refer to the time at which the snapshot has been taken along the collected trajectory.

2.A.6. Computed Total Bonding Energy for each Reactant/Product with Different Spin Alignments for all Catalytic Intermediates

Table A2.4. Total bonding energy E_{tot} (in kcal mol^{-1}) computed for each catalytic intermediate at the DFT level. Computational details are described in section 2.1 of chapter 2. The spin alignment of the unpaired electron on the Ru-based catalyst and NDI (↟ for α electron and ↡ for β electron) and the spin multiplicity of the system ($2S+1$) are also shown. ΔE_{int} (in kcal mol^{-1}) is the computed energy difference between different spin alignments and is calculated with respect to the lowest energy spin state for each catalytic step.

Step		Intermediate	$2S+1$	E_{tot}	ΔE_{int}
1st	Reactant	$[Ru^{II}–OH_2]^{2+}–NDI^{+\bullet}$ ↟	2	−13408.4	
	Product	$[Ru^{III}–OH]^{2+}–NDI$ ↟	2	−13424.2	
2nd	Reactant	$[Ru^{III}–OH]^{2+}–NDI^{+\bullet}$ ↟ ↡	1	−13292.1	0
		$[Ru^{III}–OH]^{2+}–NDI^{+\bullet}$ ↟ ↟	3	−13292.0	0.1
	Product	$[Ru^{IV}=O]^{2+}–NDI$ ↟ ↡	1	−13298.1	7.5
		$[Ru^{IV}=O]^{2+}–NDI$ ↟ ↟	3	−13305.6	0
3rd	Reactant	$[Ru^{IV}=O]^{2+}–NDI^{+\bullet}$ ↟ ↟ ↡	2	−13173.6	0
		$[Ru^{IV}=O]^{2+}–NDI^{+\bullet}$ ↟ ↡ ↟	2	−13167.6	6.0
	Product	$[Ru^{III}–OOH]^{2+}–NDI$ ↟	2	−13532.4	
4th	Reactant	$[Ru^{III}–OOH]^{2+}–NDI^{+\bullet}$ ↟ ↡	1	−13400.9	0
		$[Ru^{III}–OOH]^{2+}–NDI^{+\bullet}$ ↟ ↟	3	−13400.3	0.6
	Product	$[Ru^{II}–OO]^{2+}–NDI$ ↟ ↡	1	−13421.4	9.4
		$[Ru^{II}–OO]^{2+}–NDI$ ↟ ↟	3	−13430.8	0

2.A.7. Combination of Free Energy Profiles along the Reaction Coordinate of Route ① and ②

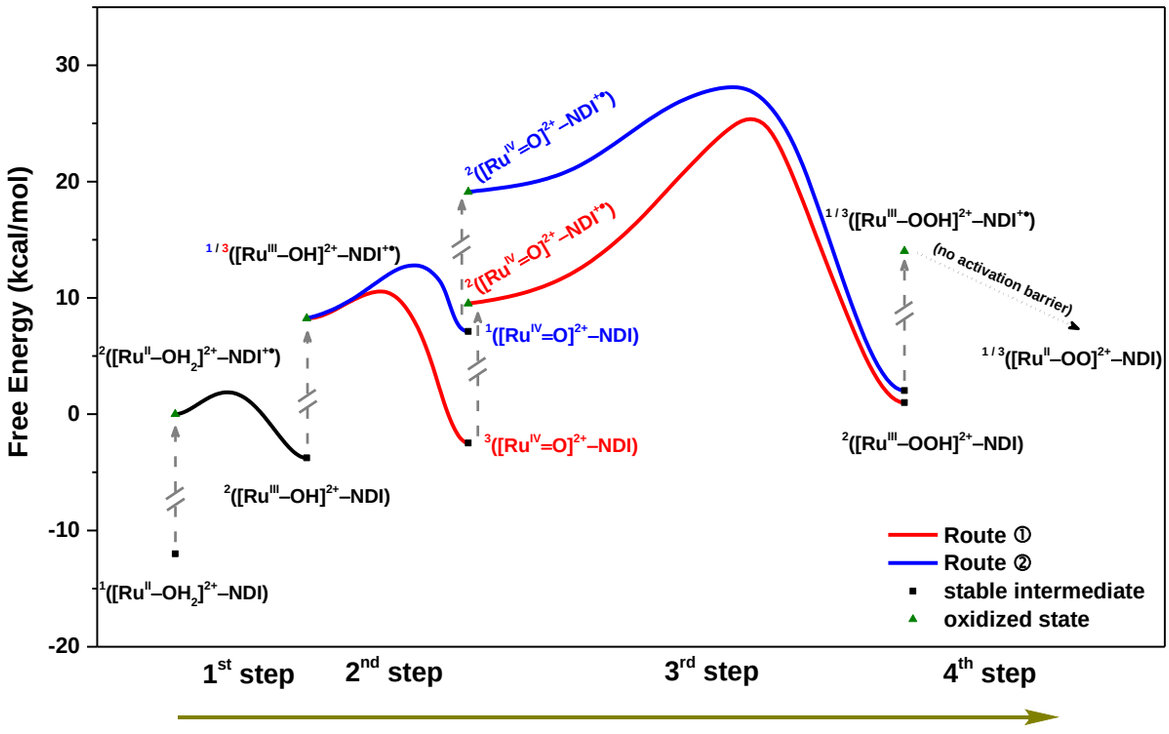

Figure A2.8. Combination of free energy profiles computed from thermodynamic integration for all steps in the catalytic cycle. For the first step (black line) only one spin state is possible. For the second and third step two different spin alignments are considered: route ① (red line) and route ② (blue line). The 4th step (black dotted arrow) is found to proceed spontaneously at room temperature for both parallel (S = 1) and antiparallel (S = 0) spin alignments, which implies no significant activation barrier. The black squares indicate the stable intermediates, while the green triangles correspond to the supramolecular complex after photooxidation of the NDI dye, leading to $NDI^{+\bullet}$. The dashed grey break arrow (not in scale) indicates the change in energy due to the photoinduced electron transfer from the NDI to the semiconductor. For the second and fourth step the two possible spin alignments after photooxidation are found to be essentially degenerate (see **Table A2.4**). The product $^{2}([Ru^{III}–OOH]^{2+}–NDI)$ at the end of the third step can be only in the S = 1/2 state. The small free energy difference found between the two routes is due to statistical/numerical errors in the thermodynamic integration procedure.

2.A.8. The Results with Antiparallel Spin Alignment on NDI along the MD Trajectories of the fourth Catalytic Step in Route ②

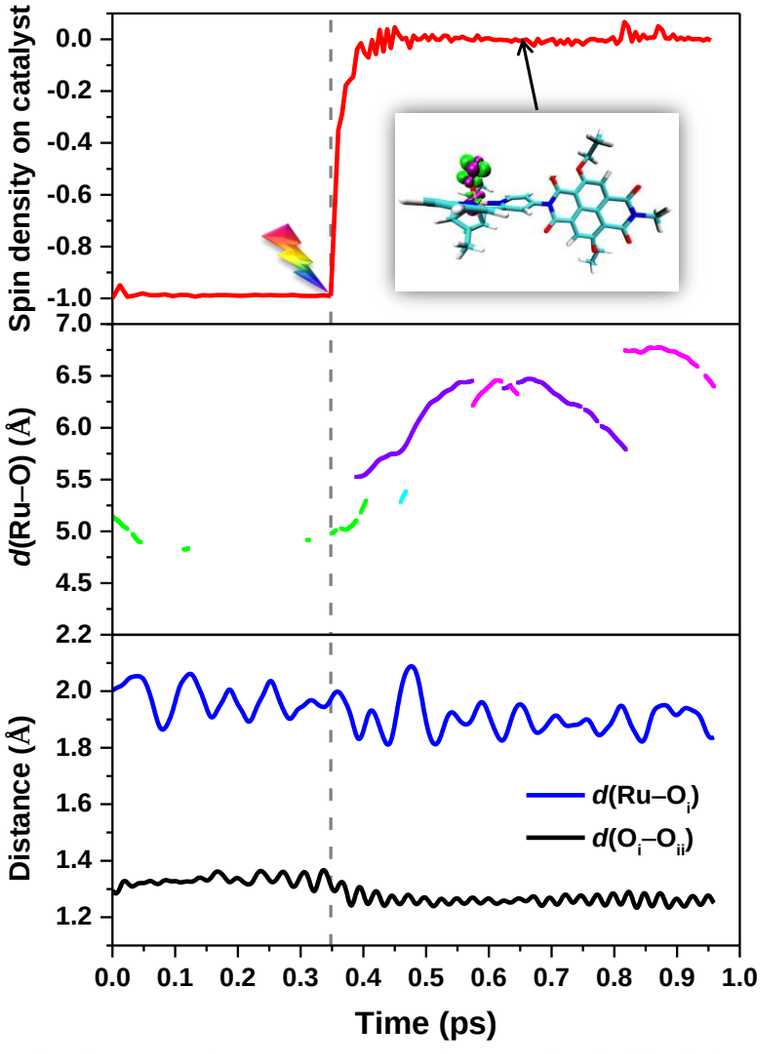

Figure A2.9. (top) The spin density integrated over the half of the simulation box including the catalyst before and after the photoinduced electron injection, which is mimicked by removing one electron from the system at 0.36 ps (indicated by the grey dotted line) to generate an oxidized $^1([Ru^{III}–OOH]^{2+}–NDI^{+\bullet})$ in the S = 0 state (see Scheme 2.1). The inset shows the spin density isosurface computed at a snapshot taken at ~0.66 ps, clearly indicating that one unpaired α electron (green spin density isosurface) and one unpaired β electron (purple spin density isosurface) are localized on the catalyst. (middle) The distance between Ru and H_3O^+ measured for the FMD simulations. According to the simulations, the proton primarily bonds to three oxygens (green, purple and magenta). (bottom) Time evolution of the geometrical parameter d(Ru–O_i) (blue line) and d(O_i–O_{ii}) (black line) along the FMD trajectory (see labeling in Scheme 2.2c).

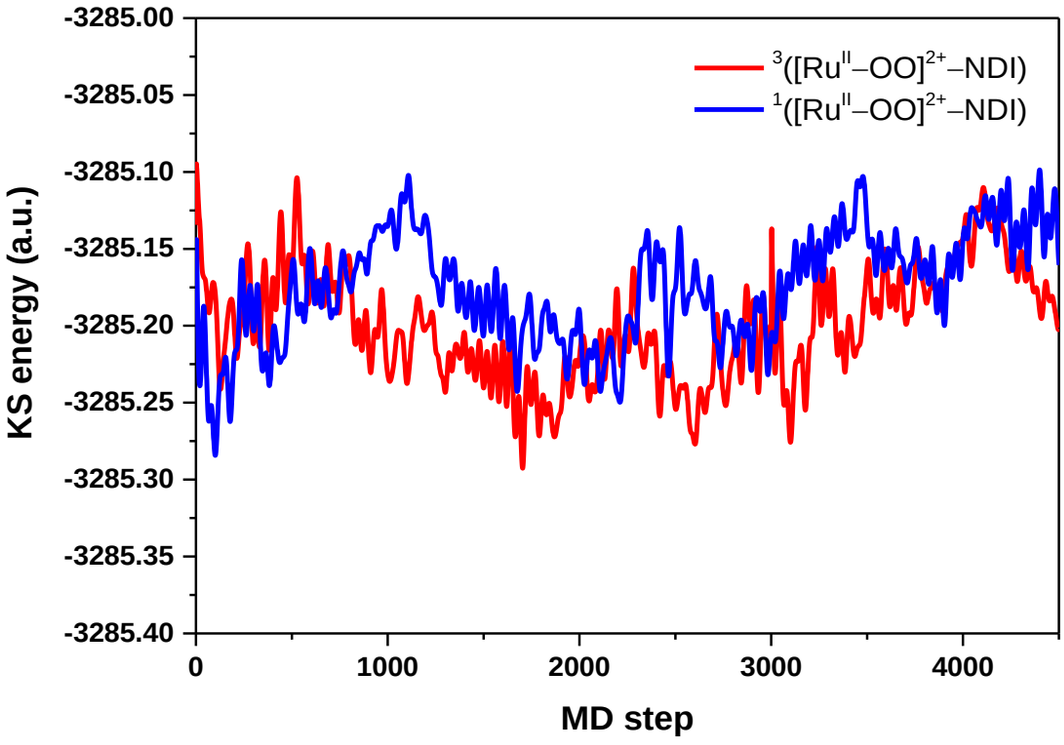

Figure A2.10. Time evolution of the KS energy of the product intermediates ^{3}([Ru^{II}–OO]$^{2+}$–NDI) (red line) and ^{1}([Ru^{II}–OO]$^{2+}$–NDI) (blue line) along the FMD trajectories after the fourth catalytic step. Although large fluctuations are observed during the MD simulations, the intermediate ^{3}([Ru^{II}–OO]$^{2+}$–NDI) indicates a relatively more stable product much lower in energy most of the time compared to the ^{1}([Ru^{II}–OO]$^{2+}$–NDI).

Table A2.5. Time-averaged KS energy of the product intermediates ^{3}([Ru^{II}–OO]$^{2+}$–NDI) and ^{1}([Ru^{II}–OO]$^{2+}$–NDI) and the energy difference between them (ΔE_{int}) along the FMD trajectories after the fourth catalytic step. The triplet state is on average almost 1 eV lower in energy than the singlet state.

2*S*+1	[Ru^{II}–OO]$^{2+}$–NDI	**KS energy (eV)**	**ΔE_{int} (eV)**
3	↑ ↑	–89395.046	0.962
1	↑ ↓	–89394.084	

2.A.9. Spin Density Integrated on the Catalyst and Time Evolution of the Dihedral Angle ∠C1–N1–C2–C3 along the MD Trajectories of each Catalytic Step in Route ①

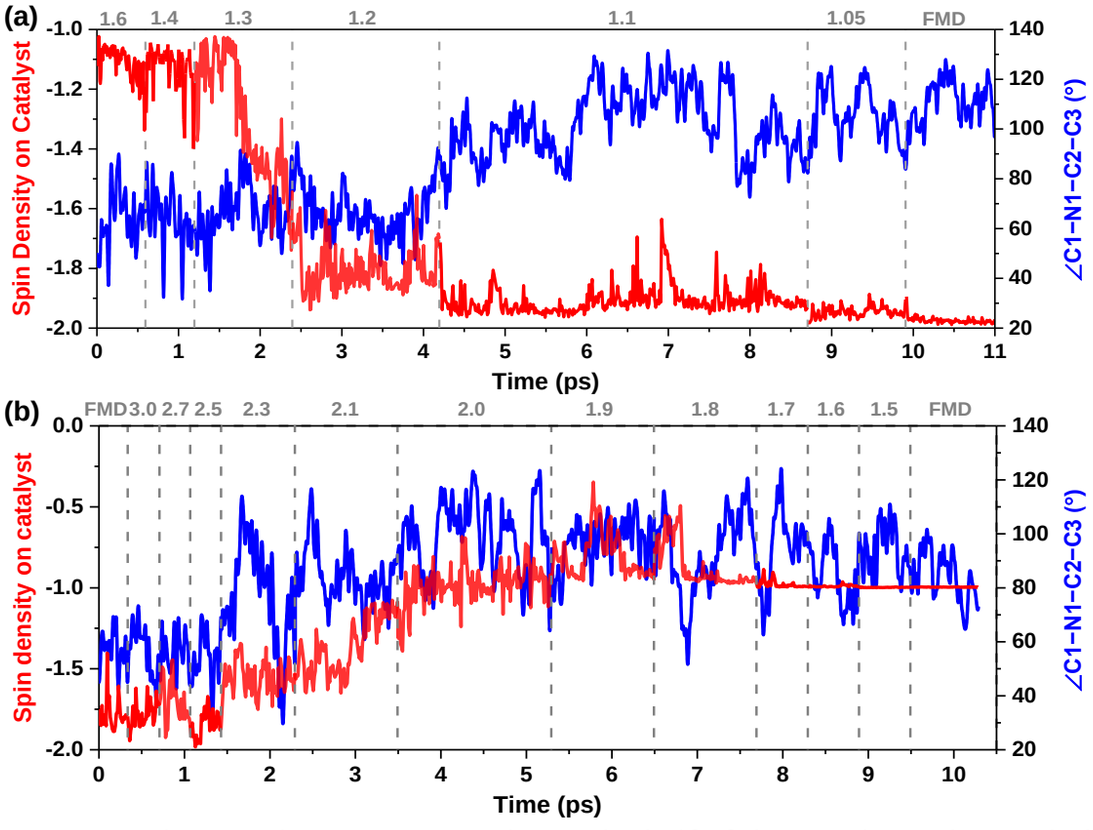

Figure A2.11. The spin density integrated over the half of the simulation box including the catalyst (red line) and time evolution of the geometrical parameter dihedral angle ∠C1–N1–C2–C3 (blue line) along the MD trajectories of (a) the second and (b) the third catalytic step (see labelling in Scheme 2.1), respectively. An integrated spin density value of –1 corresponds to one unpaired α electron. The value of the constrained reaction coordinate applied in the MD simulations for the second (a) and third (b) steps is noted in grey.

2.A.10. References

[1] Te Velde, G.; Bickelhaupt, F. M.; Baerends, E. J.; Fonseca Guerra, C.; van Gisbergen, S. J. A.; Snijders, J. G.; Ziegler, T. *J. Comput. Chem.* **2001**, *22*, 931-967.

[2] ADF2017, SCM, Theoretical Chemistry, Vrije Universiteit, Amsterdam, The Netherlands, http://www.scm.com.

[3] Klamt, A. *J. Phys. Chem.* **1995**, *99*, 2224-2235.

[4] Klamt, A.; Jonas, V. *J. Chem. Phys.* **1996**, *105*, 9972-9981.